Chemical Engineering Journal 496 (2024) 153719

Contents lists available at ScienceDirect

Chemical Engineering Journal

journal homepage: www.elsevier.com/locate/cej

Review

Advances, mechanisms and applications in oxygen evolution electrocatalysis of gold-driven

Tong Liu [a,1], Jianwei Lu [b,1], Zhihao Chen [a,b], Zhihong Luo [c], Yurong Ren [a], Xiangqun Zhuge [a], Kun Luo [a,*], Guogang Ren [d], Weiwei Lei [b,*], Dan Liu [b,*]

[a] School of Materials Science and Engineering, Changzhou University, Changzhou 213164, PR China
[b] School of Science, STEM College, RMIT University, 124 La Trobe Street, Melbourne, VIC, 3000, Australia
[c] College of Materials Science and Engineering, Guilin University of Technology, Guilin 541004, PR China
[d] University of Hertfordshire, Hatfield, Hertfordshire, AL10 9AB, UK

ARTICLE INFO

Keywords:
Oxygen evolution reaction
Electrocatalysis
Gold
Advance
Mechanism

ABSTRACT

The oxygen evolution reaction (OER) plays a crucial role in electrochemical energy storage and conversion. Among different metal elements, gold (Au) stands out due to its high electronegativity and remarkable catalytic properties, especially in nanoscale size. In this review, we aim to comprehensively analyze the oxygen electrocatalytic performance of nanosized Au, including the influence of the crystal surface, morphology, substrate materials of Au nanoparticles, size and ligands of Au nanoclusters, and Au single atoms on oxygen electrocatalysis. By exploring the catalytic performance of noble metals, non-noble metals, oxides, hydroxides/oxyhydroxides/layered double hydroxides, sulfides, phosphides, nitrides, and selenides through the integration of nanosized Au, which offers valuable insights for enhancing the OER efficiency. These effects can be attributed to two mechanisms: i) adsorbate evolution mechanism (AEM) and ii) lattice oxygen mechanism (LOM), where the nanosized Au changed the electronic structure of the catalysts and improved the adsorption of reaction intermediates to accelerate electron transfer process or exerts the synergistic effect between metallic Au and oxygen vacancies. For instance, Au-driven OER catalysts can be widely used in zinc-air batteries and water splitting in the future.

1. Introduction

With the continuous growth of global energy demand and the gradual deterioration of the environment, renewable energies such as wind and solar energies have aroused extensive concern and interest [1]. However, these sustainable energies are usually intermittent, with a time interval between supply and demand [2–5]. Therefore, efficient energy conversion and storage method is designed to realize the rational use of sustainable energy, including water splitting, fuel cells, rechargeable metal-air batteries, and other technologies [6–9]. These energy conversion and storage systems usually suffer from the slow kinetics of gas-involved electrochemical reactions, including oxygen reduction reaction (ORR), oxygen evolution reaction (OER), and hydrogen evolution reaction (HER),[10–12] among which ORR and OER contain complex multi-step electron/proton transfer processes in connection with the adsorption of different oxygen intermediates. At present, industrial oxygen electrocatalysts are still highly dependent upon platinum group metals, such as platinum (Pt), iridium (Ir), and ruthenium (Ru) based catalysts, especially under acidic conditions. However, the high cost, low crustal reserves, and catalyst poisoning significantly hinder their large-scale commercialization [1]. Au was once considered to be chemically inert [13]. Since Haruta et al revealed the excellent catalytic activity for CO oxidation on supported Au nanoparticles (NPs) in the 1980 s, the applications of Au-based catalysts have been extensively explored [14]. For example, Hutchings proved that supported Au NPs can catalyze the hydrochlorination of acetylene to produce vinyl chloride monomer [15]. Karra et al demonstrated the electrocatalytic oxidation of glucose catalyzed by Au NPs, where the irregular Au NPs exhibited higher activity than the spherical NPs [16]. Nanosized Au was also employed in the electrocatalytic reduction of N_2 to NH_3, in which the Faraday efficiency of the Au nanocages was increased by three times compared with Au nanocubes [17]. Au-based

* Corresponding authors.
E-mail addresses: luokun@cczu.edu.cn (K. Luo), weiwei.lei@rmit.edu.au (W. Lei), dan.liu@rmit.edu.au (D. Liu).
[1] **First authors:** Tong Liu and Jianwei Lu.

https://doi.org/10.1016/j.cej.2024.153719
Received 21 April 2024; Received in revised form 18 June 2024; Accepted 2 July 2024
Available online 3 July 2024

catalysts have demonstrated remarkable activity and stability in oxygen electrocatalysis, particularly in the ORR. However, the OER activity of nanosized Au is relatively low due to its limited ability to adsorb oxygen-containing intermediates. Despite ongoing debates about the electrocatalytic mechanisms involved, Au-based electrocatalysts are widely recognized as highly promising alternatives to platinum catalysts [18].

In recent years, so many research papers about Au-driven electrocatalysts have been published [19–21]. Alternatively, Au can be utilized to improve the effectiveness of other catalysts by altering their electronic structure. This adjustment enhances catalytic activity and selectivity, while also providing increased resistance to external poisoning and internal decomposition of the catalysts [22–26]. Recent studies demonstrated that incorporating nanosized Au could significantly enhance the performance of oxygen electrocatalysts, particularly in the oxygen evolution reaction process [27]. However, OER is a complex multi-step electron–proton transfer process, accompanied by the adsorption of different oxygen intermediates. The enhancement mechanism of Au in OER process is very complex. We have not yet seen any review literature regarding to this theme. In fact, our work provides a concise overview of current progress in understanding the oxygen electrocatalytic properties of nanosized Au, including crystal surface, morphology, substrate materials of Au NPs, size and ligands of Au nanoclusters (NCs), single atoms. Then, the synergistic effects of the incorporated Au are emphasized in enhancing the OER catalytic performance of noble metals, non-noble metals, oxides, hydroxides/oxyhydroxides/ layered double hydroxides, sulfides, phosphides, nitrides, and selenides. At the same time, the ORR and HER performance of the catalyst has also been improved. Additionally, this work delves into the mechanistic insights behind the enhanced OER catalytic performance achieved through the incorporation of Au and discusses the relevant applications of these Au-driven electrocatalysts.

2. Oxygen electrocatalysis of nanosized Au

For ORR and OER, the reaction process is similar, however, the reaction direction is opposite. Both processes involve reactant adsorption, electron transfer and desorption. Among them, adsorption energy of the reactive intermediates is well known as the most significant descriptor of the electrochemical reactions [28–30]. It is worth noting that ORR and OER have the same reaction intermediates. The presence of oxygen electrocatalysts is essential for both reaction processes. According to d-band theory, the varying geometry and electronic structure results in the restructuring of the d-band in active metal and a shift of the d-band center. Dropping the d-band center from the Fermi level will cause more anti-bonding states and lower adsorption of the reactive intermediates. On the other hand, increasing the d-band center will arouse more empty anti-bonding states and higher adsorption of the reactive intermediates [31–33]. The Sabatier principle indicates that a volcanic relationship exists between catalytic activity and adsorption energy, in which adsorption energy whether high or low leads to relatively low catalytic activity [34–36]. So, Au was not considered as an excellent catalyst, because of its weak chemisorption of oxygen on the smooth surface.

On the surface of nanoscale Au, the charge density of the highest occupied molecular orbital (HOMO) is convergent, which is conducive to the transfer of electrons to oxygen and benefits oxygen adsorption in electrocatalysis. The gap of the density states of Au NPs plays an important impact on the adsorption energy of reactants/intermediates and thus affects the following catalytic performance [37]. With the decrease in particle size, the specific surface area increases along with a large number of highly mismatched active sites, such as edges and corners [38]. As for NCs, the screening effect of adsorbents comes into being and the coordination number of metal atoms on small facets is lower than infinite ones [39]. When the size of Au is further reduced to the atomic level, the quantum size effect becomes dominant, which leads to unique electronic and catalytic properties [22].

2.1. Oxygen electrocatalysis of Au NPs

1. Crystal surfaces effect

Different crystal surfaces of Au NPs exhibit different oxygen electrocatalytic properties. Yang et al found that the Au (1 1 1) crystal plane has a good $2e^-$ reduction pathway for oxygen reduction according to the density functional theory (DFT) [40]. In contrast, experimental results showed that the Au (1 0 0) plane manifests a good $4e^-$ reduction pathway for ORR in alkaline environments. Duan et al studied the Au (1 0 0)/ water interface at constant potential via DFT and found that $*O_2H$ is more stable in alkaline media than acidic. Coadorbed water accelerates the breaking of O − O bonds, resulting in $4e^-$ reduction pathway of ORR [41]. Lu et al revealed that the octahedra Au NPs with the (1 1 1) crystal surface possess a $2e^-$ reduction pathway in ORR, the Au nanocubes with the (1 0 0) crystal surface exhibit a $4e^-$ reduction pathway of ORR in a certain potential region and the Au truncated ditetragonal prisms with the (3 1 0) follows the $4e^-$ reduction pathway in ORR throughout the entire potential range [42].

2. Morphology effects

The electrocatalytic properties of Au NPs are also associated with their morphologies [18]. Balasubramanian et al studied the ORR activity of Au nanowires (Fig. 1**a**), Au nanotriangles (Fig. 1**b**), Au NPs (Fig. 1**c**), and they found that Au nanowires have the best ORR activity (Fig. 1**d**), which derived from a large number of corners, edges and surface defects with the active (1 0 0) facets [43]. Jiang et al prepared a Boerdijk-Coxeter helix-structured ultrathin Au nanowire as an ORR electrocatalyst (Fig. 1**e-i**), where the ultrathin Au nanowires were superior to the Au nanowire array microspheres. In fact, Au NPs and 20 % Pt/C catalysts on the ORR activity, due to their one-dimensional anisotropy, rich surface atoms, and structural defects, also exhibited good stability and durability [44]. Moreover, the effect of capping ligands that are used to protect Au NPs from aggregation cannot be ignored on the reduction of active sites [45–47]. Luo et al also demonstrated that the hydrophobic ligands on the Au surface decreased the catalytic activity [45].

3. Support effects

The catalytic activity of Au-based catalysts is influenced by the choice of substrate materials. Various carbon-based materials such as graphene oxides, carbon nanotubes, carbon cloth, and carbon fibers are commonly used in electrochemical catalysis due to their robustness, high electronic conductivity, large specific surface area, and strong stability. These substrates play a crucial role in promoting electron transfer and are beneficial for enhancing catalytic activity [48]. Additionally, they contribute to the increasing of stability by modifying the electronic structure of nanosized Au catalysts. It is important to point out that the interaction between nanosized Au and carbon substrates can also affect the reaction pathway. For instance, when Au NPs are involved, the dual-electron ORR process typically leads to the generation of H_2O_2. However, the Au NPs on carbon nanotube substrates followed the direct $4e^-$ reduction pathway in alkaline media, exhibiting good ORR activity, excellent long-term cycle durability, and high methanol tolerance (Fig. 1**j**) [11].

2.2. Oxygen electrocatalysis of Au NCs

1. Size effects

Compared with Au NPs, Au NCs own a smaller size and a higher amount of surface atoms with low coordination numbers [18,49]. Chen et al deposited $Au_{25}(SC_2H_4Ph)_{18}$, $Au_{38}(SC_2H_4Ph)_{24}$ and $Au_{144}(SC_2H_4Ph)_{60}$ on porous carbon substrates and well-dispersed Au

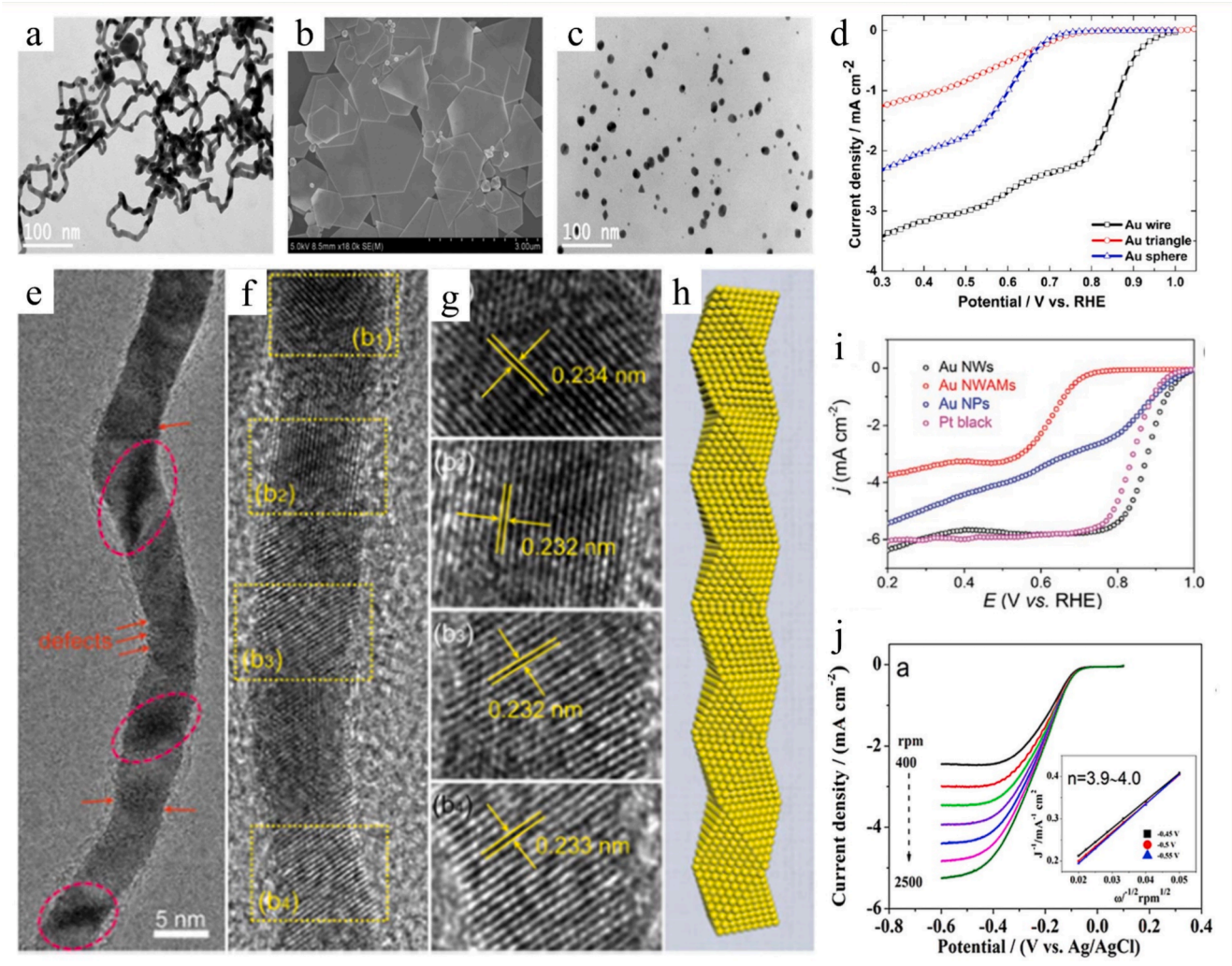

Fig. 1. (a) TEM image of Au nanowires, (b) SEM image of Au nanotriangles, and (c) TEM image of spherical Au particles, (d) ORR performance of Au nanowires, Au nanotriangles, Au particles. Reproduced with permission from ref [43]. Copyright 2017 American Chemical Society. (e-g) HRTEM images of Au nanowire, (h) schematic diagram of Boerdijk-Coxeter type helical nanowire, (i) ORR performances comparison of Au nanowires, Au nanowire-arrayed microspheres, Au NPs and 20% Pt/C. Reproduced with permission from ref [44]. Copyright 2018 Royal Society of Chemistry. (j) Rotating disk electrode polarization curves of the Au/MWNTs (insets: Koutecky-Levich plots of the catalyst). Reproduced with permission from ref [11]. Copyright 2018 John Wiley and Sons.

NCs were formed on porous carbon by pyrolysis, among which the Au_{25} nanocomposite exhibited superior ORR activity in alkaline solutions than 20 wt% Pt/C [50]. Chen et al also studied the catalytic activity of the Au_{140}, Au_{55}, Au_{25}, and Au_{11} NCs, where the catalytic activity improved with the decrease in particle size. More interestingly, the ORR pathway was shown to vary from $2e^-$ reduction pathway (Au_{140}) to $4e^-$ reduction pathway (Au_{55}, Au_{25}, Au_{11}) [51]. Kumar et al synthesized a series of Au NCs using 2-phenylethanethiolate (PET) as a capping ligand, including $Au_{25}(PET)_{18}$, $Au_{38}(PET)_{24}$, $Au_{130}(PET)_{50}$, $Au_{144}(PET)_{60}$ and $Au_{329}(PET)_{84}$. Matrix-assisted laser desorption/ionization (MALDI) mass spectrometry confirmed that Au NCs with different sizes and ligands were synthesized with high purity (Fig. 2**a**). Fig. 2**b-e** shows the ORR/OER catalytic activity increased in 0.2 M $HClO_4$ with the decrease of Au NCs' sizes. It shows that the smaller size of Au nanoclusters, the greater catalytic activity [52].

2. Ligand effects

The presence of surface ligands can affect the catalytic activity of Au NCs. For the thiol-protected Au_{28}, Au_{36}, Au_{133}, and Au_{279} NCs, Sumner et al observed that the Au_{36} NCs presented the lowest overpotential and highest $4e^-$ reduction pathway, and the order of catalytic activity, $4e^-$ reduction pathway was $Au_{36} > Au_{133} > Au_{279} > Au_{28}$ [53]. Similarly, Jones et al reported that the $Au_{65}(SR)_{29}$ NCs (SR = t-butyl thiol) owned the highest catalytic activity and $4e^-$ reduction pathway of up to 80 % among the $Au_{23}(SR)_{16}$, $Au_{30}(SR)_{18}$, $Au_{46}(SR)_{28}$ and $Au_{65}(SR)_{29}$ NCs, where the $Au_{23}(SR)_{16}$ NCs only catalyzed the formation of OH^- at a yielding rate of 53 % [54]. Moreover, Kumar et al reported that the ORR/OER catalytic activity of $Au_{25}(C_{12}T)_{18}$ ($C_{12}T$ = hexanethiolate) was significantly lower than that of $Au_{25}PET_{18}$ (PET = 2-phenylethanethiolate) and $Au_{25}(C_6T)_{18}$ (C_6T = dodecanethiolate) in 0.2 M $HClO_4$ solution (Fig. 3**b-e**). Matrix-assisted laser desorption/ionization (MALDI) mass spectrometry confirmed that Au nanoclusters with different ligands were synthesized with high purity (Fig. 3**a**). This is associated well with the thickness of the capping molecule layer, where $C_{12}T$ has a larger molecular chain than those of PET and C_6T [52].

Notably, the Au NCs charge state could also affect the reaction selectivity of Au NC-based oxygen electrocatalysts. Lu et al synthesized $Au_{25}(SC_{12}H_{25})_{18}$ with different charge states (−1, 0, and + 1) and aimed to study the effect of charge states of the $Au_{25}(SC_{12}H_{25})_{18}$ on the selectivity of ORR in alkaline media. $[Au_{25}(SC_{12}H_{25})_{18}]^{-1}$ offers the maximum H_2O_2 production and the most efficient $4e^-$ reduction pathway of ORR [55].

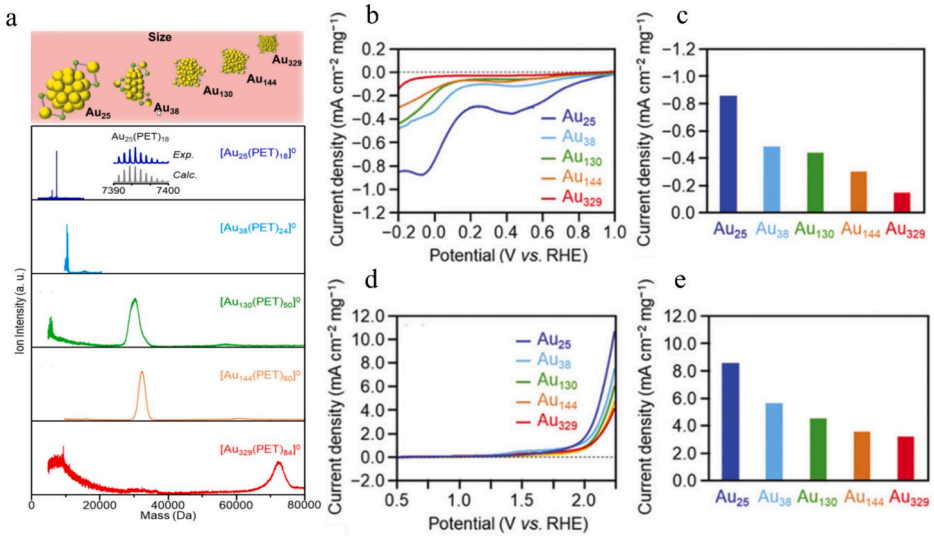

Fig. 2. (a) Matrix-assisted laser desorption time-off-light (MALDI-TOF) mass spectra of Au NCs with different sizes, (b) ORR performance and (d) OER performance of Au NCs with different sizes, (c) mass ORR activity at −0.2 V vs RHE and (e) mass OER activity at + 2.2 V vs RHE of Au NCs with different sizes. Reproduced with permission from ref [52]. Copyright 2020 Royal Society of Chemistry.

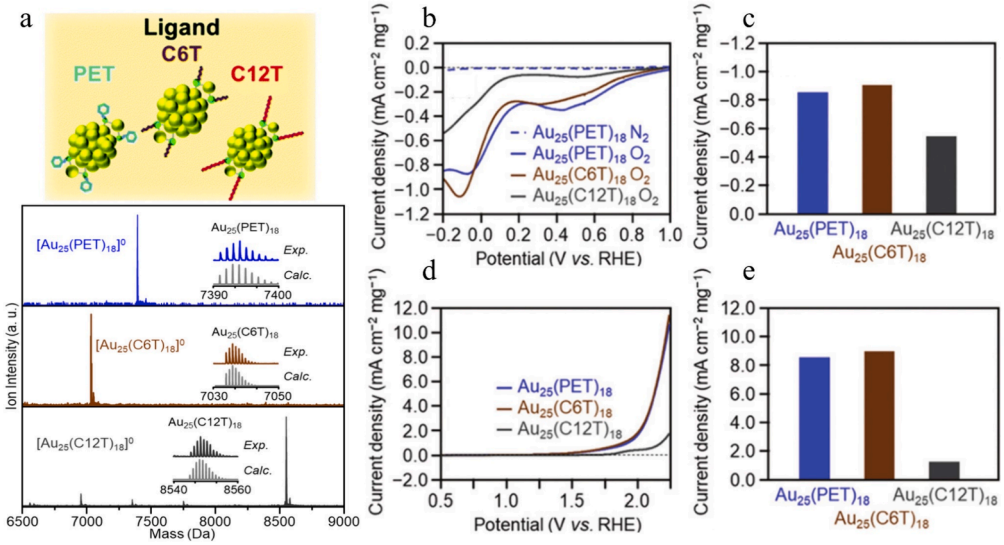

Fig. 3. (a) Matrix-assisted laser desorption time-off-light (MALDI-TOF) mass spectra of Au NCs with different ligands, (b) ORR performance and (d) OER performance of Au NCs with different ligands, (c) mass ORR activity at −0.2 V vs RHE and (e) mass OER activity at + 2.2 V vs RHE of Au NCs with different ligands. Reproduced with permission from ref [52]. Copyright 2020 Royal Society of Chemistry.

2.3. Oxygen electrocatalysis of Au single atoms

Single-atom catalyst (SAC) becomes hotspot in heterogeneous catalysis,[56] which exhibits distinctive performances for a wide variety of chemical reactions owing to the unique single-atom active center [57]. Graphite carbonitride (C_3N) has a unique triazine structure and characteristic N/C coordination pores, which provide abundant N coordination sites for stabilizing Au[58], Pt[59] and Pd[60] SAC. Chen et al synthesized the Au SAC by calcining $HAuCl_4$-C_3N_4 at 300 ℃ in a nitrogen atmosphere [61]. Wang et al obtained Au_1/C_3N_4 by reducing $HAuCl_4$ adsorbed on C_3N_4 with hydrogen and the actual loading amount of Au single atoms reached 0.15 % [62]. Liu et al synthesized the Au_1N_x SAC on C_3N_4 supported by ammonium-induced reduction and the detailed synthesizing mechanism is shown in Fig. 4**a** [63]. The high-angle annular dark field transmission electron microscopy (HAADF-TEM) in Fig. 4**b** shows metal sites circled in red, which are uniformly dispersed on the surface of g-C_3N_4 nanosheets. The intensity profiles along the line X-Y in the Magnified HAADF-STEM image (Fig. 4**c**) display that the size of uniform metal sites is ca. 0.3 nm (Fig. 4**d**), corresponding to the size of a single Au atom. The Au_1N_x catalyst exhibited a good ORR/OER bifunctional catalytic activity (Fig. 4**e**), where the OER performance of the Au_1N_x SAC is close to that of RuO_2, with the initial potential (1.4 V) lower than the RuO_2 (1.53 V). The potential of Au_1N_x SAC at the current density @10 mA cm^{-2} was 450 mV, and the Tafel slope is 112 mV dec^{-1}, as shown in Fig. 4**f**.

Density functional theory (DFT) has been widely used to predict the ORR/OER catalytic performance of single atoms catalysts. Jing et al investigated the electrocatalytic properties of the doping effect of transition metal atoms in graphene-like GaN (g-GaN) (Fig. 5**i**) by DFT calculations (Fig. 5) and the results show that Fe/g-GaN, Ni/g-GaN, and Au/g-GaN exhibit highly active in both ORR and OER electrocatalysis. Among them, the minimum OER/ORR overvoltage (0.26/0.38 eV) was

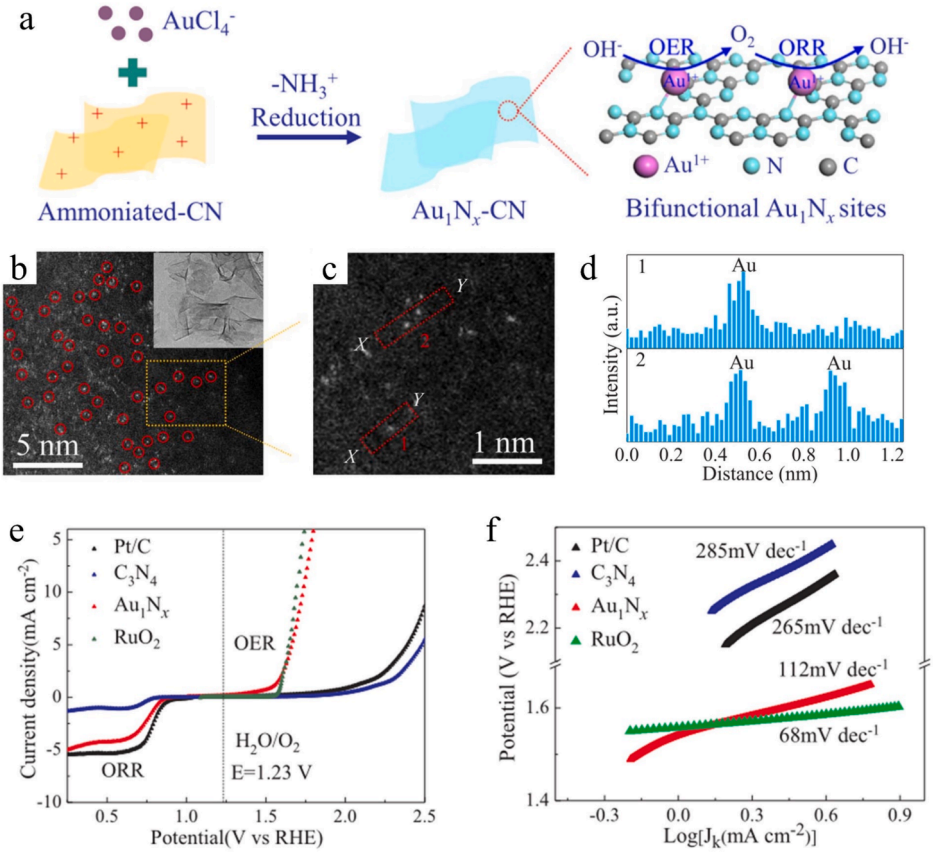

Fig. 4. (a) Schematic diagram of the synthesis and catalytic mechanism of single atoms Au_1N_x/C_3N_4 catalyst, (b) HAADF-STEM and TEM (inset) image of single atoms Au_1N_x/C_3N_4 catalyst, (c) Magnified HAADF-STEM image in (b), (d) Intensity profiles along the lines X-Y in (c), (e) ORR and OER performance of single atoms Au_1N_x/C_3N_4 catalyst, and (f) Tafel slope curve of OER. Reproduced with permission from ref [63]. Copyright 2018 Elsevier.

attributed to Ni/g-GaN and the related value of Au/g-GaN was 0.48/0.50 eV [64].

3. Oxygen evolution electrocatalysis of Au-driven

Designing efficient and long-term electrocatalysts for the OER requires a series of criteria, such as activity, stability, and practical cost [65]. Currently, noble metal catalysts such as Pt, Ir, and ruthenium (Ru) are employed for OER due to their excellent catalytic performance in both acidic and alkaline solutions. However, these noble metal catalysts are either too expensive or exhibit poor stability under high current densities [65,66]. In contrast, non-noble-metal catalysts offer a better cost-effective alternative for OER processes. These encompass a range of materials including nitrogen-doped carbon, oxides, hydroxides/oxyhydroxides/layered double hydroxides, as well as other compounds (sulfides, phosphides, nitrides, and selenides). However, the poor catalytic activity and stability in acidic media non-noble-metal catalysts limited their practical application [1].

Wang et al reviewed the research progress of embedding noble metal single atoms (Ir, Ru, and Au) into layered double hydroxides (LDHs) based single atom OER catalysts, where the atomic-level regulation is achieved through adjusting the coordination environment and the interaction with the metal-support interaction and thereby enhanced the catalytic activity [67]. Zaccaria et al proposed the incorporation of noble metal (Ir, Ru, Pd, Pt, Au) NPs or single atoms in LDHs, where less than 1 wt% of noble metals can significantly improve the OER catalytic activity of NiFe-LDHs, and can even activate the inert materials such as ZnAl-LDHs for OER catalysis [68]. In 2011, Yeo et al reported that the OER activity sequence of cobalt oxide loaded on Pt, Pd, Cu, and Co was Au > Pt > Pd > Cu > Co and the turnover frequency (TOF) of cobalt oxide on Au was three times than Ir [69]. Compared with all these noble metals, Au has the highest electronegativity that strengthens the regulation of the electronic structure of atoms nearby. Gorlin et al claimed that trace amounts of Au can significantly improve the OER activity of MnO_x [70]. There are usually two main strategies for the preparation of OER catalysts as for the introduction of Au. One is direct synthesizing method, which includes co-reduction precipitation, electrochemical deposition and so on. The other could be called element diffusion, which is usually carried out gradually, mainly including seed mediated diffusion and thermal expansion. The following part mainly focuses on the enhancement between the incorporation of Au and OER catalytic performance for various catalysts.

3.1. Noble metal OER activity of Au-driven

Wang et al synthesized the Au-Ir bimetallic catalysts on carbon paper to accelerate the OER process (Fig. 6**a**). The pristine Ir catalyst required an overpotential of 393 mV in 0.1 mol/L $HClO_4$ electrolyte to achieve a current density of 10 mA cm^{-2}, while the value for the Au-Ir catalyst was only 351 mV (Fig. 6**b**). The Tafel slope of the Au-Ir catalyst was 49.0 mV dec^{-1}, which is lower than the Ir catalyst (55.8 mV dec^{-1}) as shown in Fig. 6**c**. The incorporation of Au can also enhance the OER catalytic activity of the IrCo, IrNi, and IrCu alloys (Fig. 6**d and 6e**), in association with the characteristics of the Au/Ir interface [71]. Similarly, Ke et al synthesized the Au-Ir nano-chains through one-pot hydrothermal method, which exhibited more superior catalytic performance and stability than IrO_2, Au NPs, and Ir NPs due to the electronic interaction between Au and Ir [72]. Wang et al prepared a core–shell $Au@AuIr_2$ catalyst, which exhibited better OER catalytic activity in 0.5 mol/L H_2SO_4 solution than the commercial Ir/C catalyst, and its catalytic

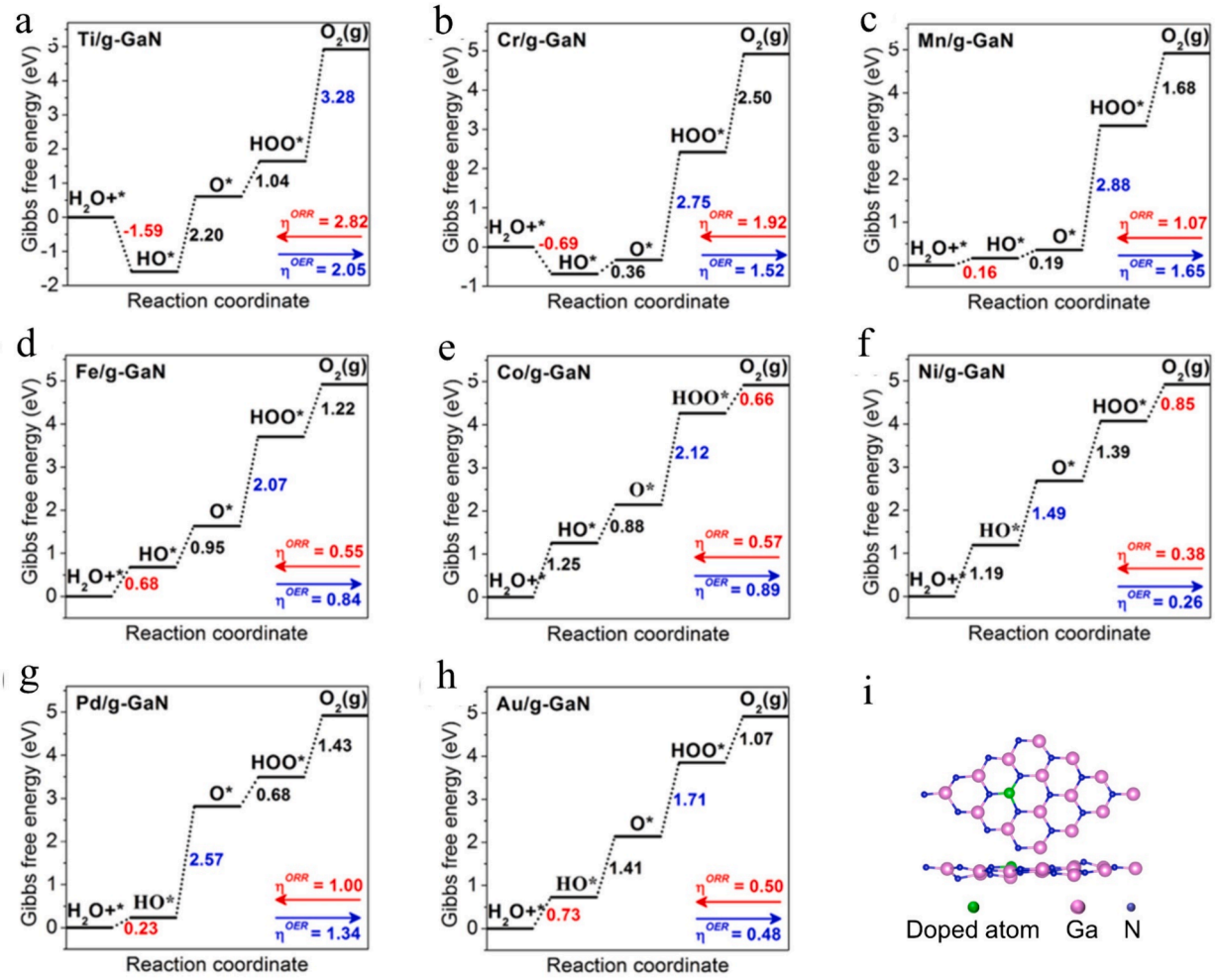

Fig. 5. Free energy step diagram of Ti/g-GaN(a), Cr/g-GaN(b), Mn/g-GaN(c), Fe/g-GaN(d), Co/g-GaN(e), Ni/g-GaN(f), Pd/g-GaN(g), Au/g-GaN(h) for the OER/ORR, (i) doping structure diagram. Reproduced with permission from ref [64]. Copyright 2021 American Chemical Society.

activity in HER was also comparable to the Pt/C catalyst. When used in water splitting, the Au@$AuIr_2$ catalyst required only 1.55 V at 10 mA cm^{-2} and the performance could be maintained for 40 h [73]. The incorporation of Au can also improve the OER activity of Ir/IrO_2 when a small amount of Au was introduced into the obtained $Au_xIr_{1-x}O_y$ nanofibers by electrospinning presented apparent enhancement on the OER catalytic activity [74].

Ru also has excellent OER catalytic activity and can significantly improve the OER and HER catalytic activity and stability in acidic media after alloying with a small amount of Au. Kwon et al reported that the AuRu alloy nanofibers manifested good OER catalytic activity in 0.5 mol/L H_2SO_4 solution, where only 1.472 V was needed to provide a current density of 10 mA cm^{-2} for water electrolysis [75]. Table 1 summarizes the recent advances in the Au-driven noble metal catalysts in the OER process.

3.2. Non-noble metal OER activity of Au−driven

The incorporation of Au into non-noble-metal catalysts for OER has proven to be beneficial in several aspects, such as modifying the electronic structure, improving the adsorption of reaction intermediates, facilitating electron transfer, and enhancing the overall reaction kinetics [77]. These improvements were achieved via the synergistic effect between Au and non-noble-metal catalysts. The following section presents an overview of the state-of-the-art advancements in research involving the combination of Au with various metals such as Ni, Co, Mn, Fe, and Cu, as well as their corresponding oxides, hydroxides, oxyhydroxides, layered double hydroxides, phosphides, nitrides, sulfides, and selenides.

3.2.1. Metals/alloys OER activity of Au-driven

Non-noble metals are utilized as catalysts for the OER in both acidic and alkaline electrolytes and they tend to experience varying degrees of corrosion. To address this issue, Irene et al synthesized stable Au-Fe nano alloys through laser ablation, which possessed better OER performance than the FeO_x [79]. Cheng et al modified the metal–organic frameworks of Fe, Co, and Ni with Au nanocrystals (Au/(FCN)MOF/NP). XPS analysis (Fig. 7**a ~ 7d**) indicated that the binding energies of Fe_{2p}, Co_{2p}, Ni_{2p} were increased by about 0.3 ~ 0.5 eV and the binding energy of Au_{4f} was decreased by 0.4 eV. The reason could be attributed to the higher electronegativity of Au and thereby increased the binding energies of the metal centers, which will pull electrons away from the non-noble metals, made the metal centers positively charged. OER testing showed that the overvoltage of the Au/(FCN)MOF/NP catalyst at 10 mA cm^{-2} was reduced by 26 mV compared with the (FCN)MOF/NP (Fig. 7**e**) and the Tafel slope was reduced by 10.4 mV dec^{-1} (Fig. 7**f**) [78].

Prussian blue analogs (PBA) are coordination polymers based on bimetallic complexation, which have good stability in acidic and alkaline electrolytes. Roger et al prepared different core–shell (NiFe, CoFe) Au@PBA catalysts, where the presence of Au nuclei significantly reduced the OER overpotential of the catalysts, and the reaction kinetics remained nearly unchanged [80]. The OER catalytic performance of Au-driven non-noble metals/alloys in previous literatures is listed in

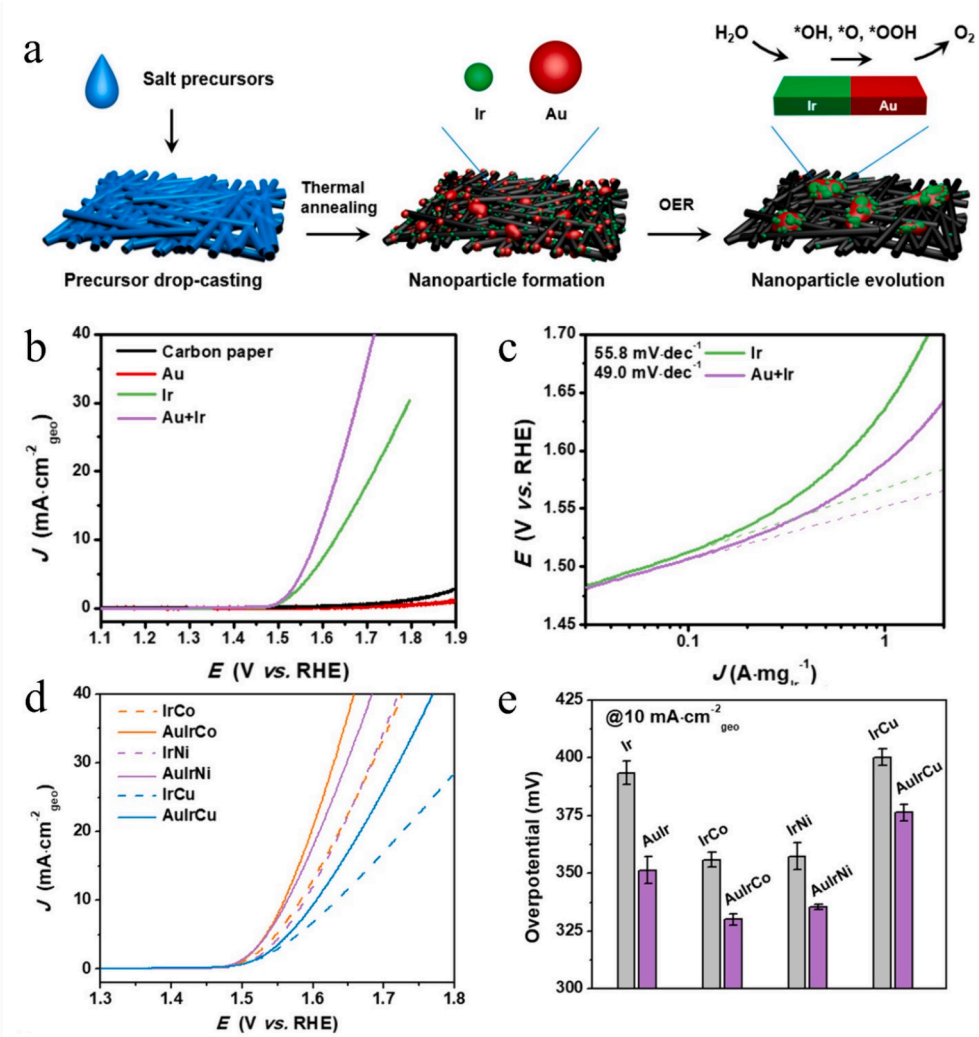

Fig. 6. (a) Scheme preparation of Au and Ir catalysts on carbon paper supports and their structural transformation into heterostructured Au-Ir particles in OER measurements, (b) OER curves and (c) Tafel curves of AuIr catalysts, (d) OER curves and (e) overvoltage diagrams at a current density of 10mA cm^{-2} of Au enhanced IrCo, IrNi, and IrCu catalysts. Reproduced with permission from ref [71]. Copyright 2021 American Chemical Society.

Table 2.

3.2.2. *Oxides OER activity of Au−driven*

Nowadays, non-noble metal oxide based on its low-cost and stability has attracted considerable attention in electrocatalytic applications [1]. Zhang et al found that the incorporation of Au NPs with CuO_x resulted in the decrease of overpotential at 10 mA cm^{-2} by 100 mV and the corresponding Tafel slope 57 mV dec^{-1} [83]. Moreover, the combination of Au NPs with Co_3O_4 led to the decrease of overpotential at 10 mA cm^{-2} by 80 mV and the Tafel slope as low as 16 $mVdec^{-1}$ [84].

The catalyst with a core–shell structure, where the core is composed of Au, exhibits excellent reaction activity. Zhuang et al synthesized a core–shell catalyst denoted as Au@Co_3O_4 shown in Fig. 8**a**. The OER activity of Au@Co_3O_4 was 7 times higher than the physical mixture of Au and Co_3O_4, which was stronger than pristine Au and Co_3O_4 nanocrystals (Fig. 8**b and 8c**) [81]. Strickler et al synthesized a group of core–shell composites (Au@M_xO_y, M = Ni, Co, Fe, and CoFe) for OER catalysis. TEM analysis in Fig. 8**d** illustrated that the Au@$CoFeO_x$ catalyst was composed of Au nucleus core and $CoFeO_x$ shell, which exhibited the best OER catalytic activity (Fig. 8**e and 8f**) than the Au@CoO_x, Au@NiO_x, and Au@FeO_x [82]. All Au-based catalysts exceed their pure metal-oxide counterparts in OER activity on both a geometric and mass activity basis, suggesting the interaction between the metallic Au and transition metal oxides. The OER catalytic performance of Au-driven non-noble-metal oxides is shown in Table 3.

3.2.3. *Hydroxides/oxyhydroxides/layered double hydroxides OER activity of Au-driven*

In this section, we provided a comprehensive overview and introduction of hydroxides, oxyhydroxides, and layered double hydroxide (LDH). Sayeed et al deposited $Co(OH)_2$ on carbon, palladium, copper, Au electrodes, and conducted OER tests in 1 mol/L NaOH. The experimental results showed the Au electrode could significantly enhance the OER performance of $Co(OH)_2$ [93]. Cai et al prepared $Co(OH)_2$ doped with Au single atoms, which manifested an overvoltage reduction of 150 mV at 10 mA cm^{-2} from $Co(OH)_2$, with a Tafel slope of 52 mV dec^{-1} [94]. Madhu et al used a wet-chemistry method to synthesize $Ni(OH)_2$ nanosheets with different Au doping amounts (different concentrations of Au^{3+}) as an OER electrocatalyst in 1 mol/L KOH solution. The overpotential of Au-doped $Ni(OH)_2$ was reduced by 82 mV at 10 mA cm^{-2}, and the Tafel slope by 31 mV dec^{-1} compared with $Ni(OH)_2$. The reason is that Au on the surface of $Ni(OH)_2$ led to a change in the electronic structure of the electroactive nickel site, which is conductive to OER electronically [95].

Zhou et al investigated the updated OER catalysts at the interfaces of metal hydroxides and Au NCs, where a series of core–shell AuNCs@M$(OH)_2$ (M = Co and Ni) tubular nanocomposites were synthesized. AuNCs@M$(OH)_2$ manifested more than 10-times current densities of the

Table 1
Au-driven noble metal catalysts in the OER process.

Catalyst	Electrolyte	Overpotential (mV vs RHE)	Overpotential decrement (mV)	Tafel slope (mV/dec)	Ref
AuIr	0.1 mol/L $HClO_4$	351@10 mA cm^{-2}	42	49.0	[71]
Ir	0.1 mol/L $HClO_4$	393@10 mA cm^{-2}		55.8	
AuIrCo	0.1 mol/L $HClO_4$	330@10 mA cm^{-2}	25	–	
IrCo	0.1 mol/L $HClO_4$	355@10 mA cm^{-2}		–	
AuIrNi	0.1 mol/L $HClO_4$	335@10 mA cm^{-2}	22	–	
IrNi	0.1 mol/L $HClO_4$	357@10 mA cm^{-2}		–	
AuIrCu	0.1 mol/L $HClO_4$	376@10 mA cm^{-2}	24	–	
IrCu	0.1 mol/L $HClO_4$	400@10 mA cm^{-2}		–	
Au@$AuIr_2$	0.5 mol/L H_2SO_4	261@10 mA cm^{-2}	63	58.3	[73]
Ir/C	0.5 mol/L H_2SO_4	324@10 mA cm^{-2}		69.6	
IrO_2	0.5 mol/L H_2SO_4	356@10 mA cm^{-2}		73.3	
Au@Ir NRB	0.5 mol/L H_2SO_4	296@10 mA cm^{-2}	57	51.4	[76]
Ir/C	0.5 mol/L H_2SO_4	353@10 mA cm^{-2}		74.3	
IrO_y-70	0.5 mol/L H_2SO_4	257@10 mA cm^{-2}		57.2	[74]
$Au_{0.05}Ir_{0.95}O_y$-70	0.5 mol/L H_2SO_4	255@10 mA cm^{-2}	2	60.0	
$Au_{0.10}Ir_{0.90}O_y$-70	0.5 mol/L H_2SO_4	250@10 mA cm^{-2}	7	56.8	
$Au_{0.33}Ir_{0.67}O_y$-70	0.5 mol/L H_2SO_4	270@10 mA cm^{-2}	−13	49.6	
IrO_y-50	0.5 mol/L H_2SO_4	246@10 mA cm^{-2}		57.4	
$Au_{0.05}Ir_{0.95}O_y$-50	0.5 mol/L H_2SO_4	243@10 mA cm^{-2}	3	58.0	
$Au_{0.10}Ir_{0.90}O_y$-50	0.5 mol/L H_2SO_4	241@10 mA cm^{-2}	5	55.2	
$Au_{0.33}Ir_{0.67}O_y$-50	0.5 mol/L H_2SO_4	267@10 mA cm^{-2}	−21	49.5	
Ir/C	0.5 mol/L H_2SO_4	270@10 mA cm^{-2}		59.7	
AuRu NF_s	0.5 mol/L H_2SO_4	154@10 mA cm^{-2}	13	34.2	[75]
Ru NF_s	0.5 mol/L H_2SO_4	167@10 mA cm^{-2}		34.6	
Au/RuO_2 NF_s	0.5 mol/L H_2SO_4	188@10 mA cm^{-2}	−5	41.4	
RuO_2 NF_s	0.5 mol/L H_2SO_4	183@10 mA cm^{-2}		42.5	
Au NPs	0.5 mol/L H_2SO_4	1129@10 mA cm^{-2}		219.2	
AuIr NCs	1 mol/L KOH	310@10 mA cm^{-2}	20	52.94	[72]
Au NP	1 mol/L KOH	680@10 mA cm^{-2}		449.5	
Ir NP	1 mol/L KOH	330@10 mA cm^{-2}		78.8	
IrO_2	1 mol/L KOH	332@10 mA cm^{-2}		82.69	

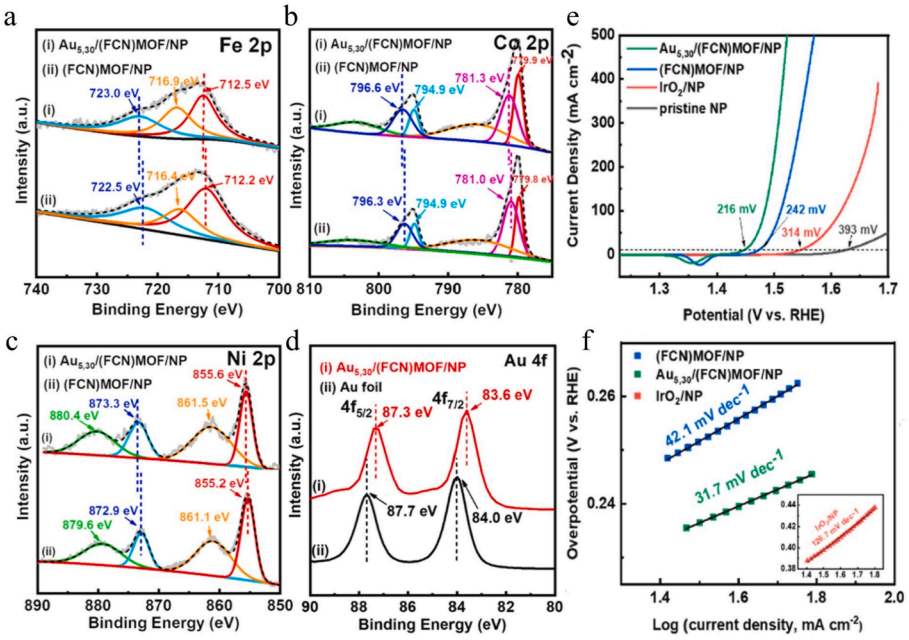

Fig. 7. HR-XPS spectra of $Au_{5.30}$/(FCN)MOF/NP and (FCN)MOF/NP: (a) Fe 2p, (b) Co 2p, (c) Ni 2p, and (d) Au 4f, (e) OER curves and (f) Tafel curves. Reproduced with permission from ref [78]. Copyright 2021 Elsevier.

corresponding $M(OH)_2$ catalysts at the overvoltage of 0.42 V vs RHE, among which the AuNCs@$Ni(OH)_2$ exhibited the best OER catalytic stability [96]. The synergistic effect of multiple metals can further improve catalytic performance. Zhang et al directly electrodeposited Pr-doped NiFeCo hydroxide on Au-plated nickel foam (NF), which also exhibited a high OER catalytic activity, with a Tafel slope of 28 mV dec^{-1} in a 1 mol/L KOH electrolyte, a reduction of 228 mV at the overpotential of 60 mA cm^{-2}, and stability for 10 h. Au-NiFeCoPr has the lowest Tafel slope in existing literature due to the synergistic effect of Au atoms on various metal elements [97]. The OER catalytic performance of Au-driven non-noble metal hydroxides is shown in Table 4.

Liu et al studied the catalytic activity of NiFeOOH modified with Au NPs in OER process. As shown in Fig. 9**a** ∼ **9c**, Fe doping significantly improved the catalytic activity of the NiOOH. Further modified with Au

Table 2
Recent progress of the Au-enhanced non-noble metals/alloys on the OER catalytic performance.

Catalyst	Electrolyte	Overpotential (mV vs RHE)	Overpotential decrement (mV)	Tafel slope (mV/dec)	Ref
$Au_{0.89}Fe_{0.11}$	1 mol/L KOH	800@10 mA cm^{-2}	400	163	[79]
FeO_x	1 mol/L KOH	1200@10 mA cm^{-2}		350	
Au/(FCN) MOF/NP	1 mol/L KOH	216@10 mA cm^{-2}	26	31.7	[78]
(FCN)MOF/NP	1 mol/L KOH	242@10 mA cm^{-2}		42.1	
Au@NiFe PBA	1 mol/L KOH	375@10 mA cm^{-2}	90	89	[80]
NiFe PBA	1 mol/L KOH	465@10 mA cm^{-2}		92	
Au@CoFe PBA	1 mol/L KOH	357@10 mA cm^{-2}	48	63	
CoFe PBA	1 mol/L KOH	405@10 mA cm^{-2}		66	

NPs, the OER catalytic activity became even higher. In fact, density functional calculations for Au@NiFeOOH found that the catalytic active center shifted towards the Au NP interface. As a result, the overpotential at 10 mA cm^{-2} was decreased by 31 mV, and the Tafel slope by 5.35 mV dec^{-1} [101]. Sun et al studied the OER performance of Cr doped NiFe oxyhydroxides nanosheets, Cr further improved the OER performance of Au/NiFe, with an ultra-low Tefel slope of 33 mV dec^{-1} [102]. The OER catalytic performance of Au-driven non-noble metal oxyhydroxides was shown in Table 5.

Layered double hydroxide (LDH) consists of stacked metal hydroxide nanosheets, along with embedded water molecules and anions, exhibiting excellent OER activity. Zhu et al synthesized AuNiFe LDH on nickel foam and tested its OER performance. AuNiFe LDH OER activity at a current density of 500 mA cm^{-2} decreased by 44 mV and the Tafel slope decreased by 22.7 mV dec^{-1}, compared with pure NiFe LDH. The synergistic effect between Au NPs and NiFe LDH enhances NiFe LDH@Au [103]. Zhang et al loaded 0.4 wt% single atom Au on NiFe LDH, and successfully increased the OER catalytic activity by six times. AuNiFe LDH the OER activity at a current density of 10 mA cm^{-2} decreased by 26 mV and the Tafel slope decreased by 24 mV dec^{-1}, compared with NiFe LDH [104].

Kitano et al focus on nanosheets of unilamellar layered double hydroxides (ULDHs) to increase the number of contact areas between Au clusters and LDHs. They studied the effect of Au clusters on the OER performance of unilamellar NiFe, NiCo, and NiMn hydroxides (Fig. 10**a** ~ **10c**) and found that Au has really improved catalytic activity on hydroxides. In addition, Fig. 10**c** showed that an overvoltage with a current density of 10 mA cm^{-2} decreased first and then increased with the addition of Au. This result demonstrates that Au clusters lead to charge transfer at the heterogeneous interface of hydroxides, which regulates the oxidation state of trivalent metals, and proposes an interface-based O-O coupling mechanism [105]. The OER activity of Au-driven non-noble-metal LDHs is shown in Table 6.

3.2.4. Sulfides OER activity of Au-driven

Tran et al synthesized the Au/Co_xS_y nanocomposites through a two-step method (Fig. 11**a**). The first step was to integrate Au nanodots into the structure of ZIF-67 by reducing the inserted Au ions. Then, Au/Co_xS_y nanohybrids were synthesized through a solution-based etching process (Fig. 11**b** ~ **11e**). The Au/Co_xS_y manifested better OER activity than the Co_xS_y (Fig. 11**f**), with an overpotential reduction of 80 mV at 10 mA cm^{-2}, and a reduction of 16 mV dec^{-1} on the Tafel slope [108].

Duan et al designed a group of transition metal sulfide nanostructures, including core–shell Au-$CoNi_2S_4$, Au-NiS, Au-Co_3S_4, and pristine $CoNi_2S_4$ NPs. Among them, Au-$CoNi_2S_4$ has the optimal OER catalytic activity (Fig. 11**g**), which reduced the overvoltage at 10 mA cm^{-2} by 80 mV and the Tafel slope by 16 mV dec^{-1} compared with $CoNi_2S_4$ [111]. The OER catalytic performance of Au-driven non-noble metal sulfides is listed in Table 7.

3.2.5. Phosphides OER activity of Au-driven

Zhang et al reported that the core–shell Au@Co_2P NPs exhibited an overvoltage of 321 mV at 10 mA cm^{-2} in 1 mol/L KOH solution, which was 95 mV lower than that of the Co_2P. The Tafel slope of the Au@Co_2P was 57 mV dec^{-1}, which was also much lower than the Co_2P (101 mV dec^{-1}) [116].

Cai et al prepared the Au@Ni_2P core–shell catalyst (Fig. 12**a**). When calcined at 350 °C or higher, Au nuclei began to diffuse or dissolve into

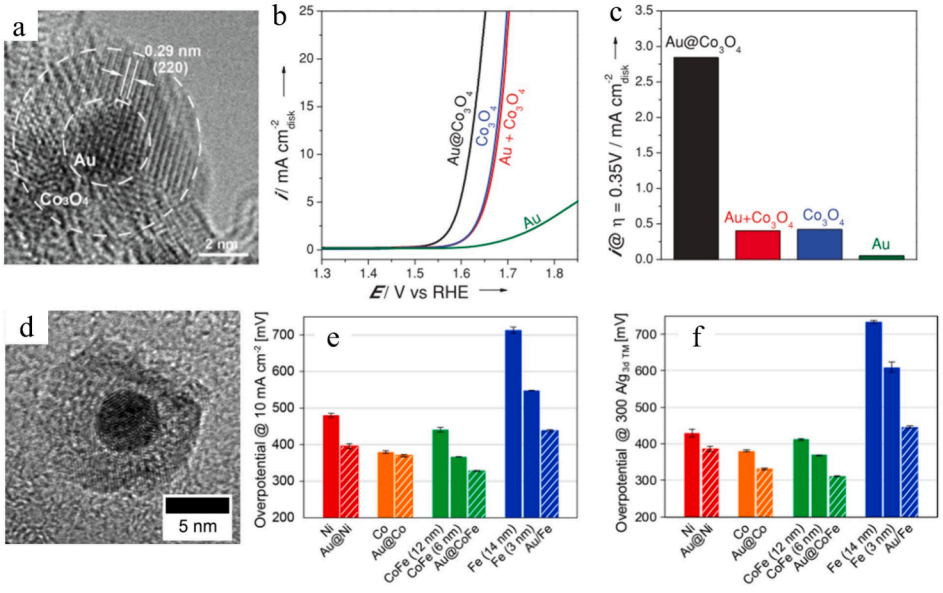

Fig. 8. (a) HRTEM image of the Au@Co_3O_4 catalyst, (b) OER test, (c) current density at an overvoltage of 0.35 V. Reproduced with permission from ref [81]. Copyright 2014 John Wiley and Sons. (d) TEM image of the Au@$CoFeO_x$ catalyst, (e) the overpotential at a current density of 10 mA cm^{-2}, and (f) the overpotential at a mass activity of 300 A/g. Reproduced with permission from ref [82]. Copyright 2017 American Chemical Society.

Table 3
OER catalytic performance of Au-driven non-noble metal oxides.

Catalyst	Electrolyte	Overpotential (mV vs RHE)	Overpotential decrease(mV)	Tafel slope (mV/dec)	Ref
Fe_3O_4@Au	0.1 mol/L KOH	810@10 mA cm^{-2}	640	95	[85]
Fe_3O_4	0.1 mol/L KOH	1450@10 mA cm^{-2}		241	
Au	0.1 mol/L KOH	1566@10 mA cm^{-2}		276	
Au-CuO_x	1 mol/L Na_2CO_3 (pH = 11.4)	380@10 mA cm^{-2}	100	74	[83]
CuO_x	1 mol/L Na_2CO_3 (pH = 11.4)	480@10 mA cm^{-2}		130	
Au/MnO_2	0.5 mol/L KOH	386@1mA cm^{-2}	10	64	[86]
MnO_2	0.5 mol/L KOH	396@1mA cm^{-2}		66	
Au/Mn_2O_3	0.5 mol/L KOH	309@1mA cm^{-2}	3	82	
Mn_2O_3	0.5 mol/L KOH	312@1mA cm^{-2}		84	
Au/Co_3O_4	1 mol/L KOH	225@10 mA cm^{-2}	90	61	[87]
Co_3O_4	1 mol/L KOH	335@10 mA cm^{-2}		124	
Au@Co_3O_4	1 mol/L KOH	320@10 mA cm^{-2}	80	75	[84]
Co_3O_4	1 mol/L KOH	400@10 mA cm^{-2}		91	
$AuMnO_x$	1 mol/L KOH	420@10 mA cm^{-2}	60	–	[88]
MnO_x	1 mol/L KOH	480@10 mA cm^{-2}		–	
CNTsAu@Co_3O_4	1 mol/L KOH	350@10 mA cm^{-2}	60	68	[89]
CNTs@Co_3O_4	1 mol/L KOH	410@10 mA cm^{-2}		82	
Au/MnO_2	0.1 mol/L KOH	390@10 mA cm^{-2}	240	–	[90]
MnO_2	0.1 mol/L KOH	630@10 mA cm^{-2}		–	
Au@Co_3O_4	0.1 mol/L KOH	370@10 mA cm^{-2}	60	60	[81]
Co_3O_4	0.1 mol/L KOH	430@10 mA cm^{-2}		59	
$AuCoFe_2O_4$	1 mol/L KOH	312@10 mA cm^{-2}	62	35	[91]
$CoFe_2O_4$	1 mol/L KOH	374@10 mA cm^{-2}		46.8	
$AuCoFeO_x$	1 mol/L KOH	328@10 mA cm^{-2}	113	58	[82]
$CoFeO_x$	1 mol/L KOH	441@10 mA cm^{-2}		58	
$AuNiO_x$	1 mol/L KOH	394@10 mA cm^{-2}	87	117	
NiO_x	1 mol/L KOH	481@10 mA cm^{-2}		108	
$AuCoO_x$	1 mol/L KOH	332@10 mA cm^{-2}	49	92	
CoO_x	1 mol/L KOH	381@10 mA cm^{-2}		78	
$AuFeO_x$	1 mol/L KOH	439@10 mA cm^{-2}	118	43	
FeO_x	1 mol/L KOH	557@10 mA cm^{-2}		85	
$AuZnCo_2O_4$/CNTs	1 mol/L KOH	440@10 mA cm^{-2}	30	46.2	[92]
$ZnCo_2O_4$/CNTs	1 mol/L KOH	470@10 mA cm^{-2}		47.6	
$ZnCo_2O_4$	1 mol/L KOH	480@10 mA cm^{-2}		52.7	
Au/CNTs	1 mol/L KOH	570@5 mA cm^{-2}		116.8	

Table 4
OER catalytic performance of Au-driven non-noble metal hydroxides.

Catalyst	Electrolyte	Overpotential (mV vs RHE)	Overpotential decrement (mV)	Tafel slope (mV/dec)	Ref
Au-$Co(OH)_2$	1 mol/L KOH	260@10 mA cm^{-2}	150	52	[94]
α-$Co(OH)_2$	1 mol/L KOH	410@10 mA cm^{-2}		104	
Au-$Ni(OH)_2$	1 mol/L KOH	288@10 mA cm^{-2}	82	55	[95]
$Ni(OH)_2$	1 mol/L KOH	370@10 mA cm^{-2}		86	
Au@$Ni(OH)_2$	1 mol/L KOH	262@10 mA cm^{-2}	66	74	[98]
$Ni(OH)_2$	1 mol/L KOH	328@10 mA cm^{-2}		80	
$AuCo(OH)_2$	0.5 mol/L KOH	456@10 mA cm^{-2}	84	88	[99]
$Co(OH)_2$	0.5 mol/L KOH	540@10 mA cm^{-2}		–	
$AuCo(OH)_2$	0.1 mol/L KOH	380@10 mA cm^{-2}	93	42	[100]
$Co(OH)_2$	0.1 mol/L KOH	473@10 mA cm^{-2}		53	
Au@$Co(OH)_2$	0.1 mol/L KOH	350@10 mA cm^{-2}	–-	72	[96]
$Co(OH)_2$	0.1 mol/L KOH	350@1.7 mA cm^{-2}		146	
Au@$Ni(OH)_2$	0.1 mol/L KOH	375@10 mA cm^{-2}	–-	73	
$Ni(OH)_2$	0.1 mol/L KOH	375@0.5 mA cm^{-2}		93	
$AuCo(OH)_2$	1 mol/L NaOH	360@10 mA cm^{-2}		122	[93]
Au-NiFeCoPr	1 mol/L KOH	228@60 mA cm^{-2}	17	28	[97]
NiFeCoPr	1 mol/L KOH	247@60 mA cm^{-2}		79	
NiFeCo	1 mol/L KOH	251@60 mA cm^{-2}		100	
NiFe	1 mol/L KOH	260@60 mA cm^{-2}		398	

the Ni_2P shell, in the form of Au single atoms or NCs (Fig. 12**b**). The Au@Ni_2P-350 °C exhibited the best OER catalytic activity, compared with the Au@Ni_2P, Ni_2P, Au, and commercial IrO_2 (Fig. 12**c** ~ **12d**). At the current density of 50 mA cm^{-2} in 1 mol/L KOH electrolyte, the overpotential was only 336 mV, which was 121 mV lower than the Ni_2P. The Tafel slope was measured as 58 mV dec^{-1}, which was also lower than the Ni_2P (71 mV dec^{-1}). Consequently, this indicated that the thermal diffusion of Au was conductive to enhance the catalyst activity [114].

On the one hand, the catalyst with a core–shell structure, where the core is composed of Au, exhibits excellent catalytic activity. On the other hand, the type of core–shell structure was also a key point. Xu et al investigated two kinds of Au/$Ni_{12}P_5$ catalysts; Au modified $Ni_{12}P_5$ and core–shell Au-$Ni_{12}P_5$ NPs. Both catalysts exhibit much better OER activity than pristine $Ni_{12}P_5$, indicative of the effective electronic coupling between Au and $Ni_{12}P_5$ (Fig. 12**e** ~ **12f**) [115]. The OER catalytic performance of Au-driven non-noble metal phosphides is organized in Table 8.

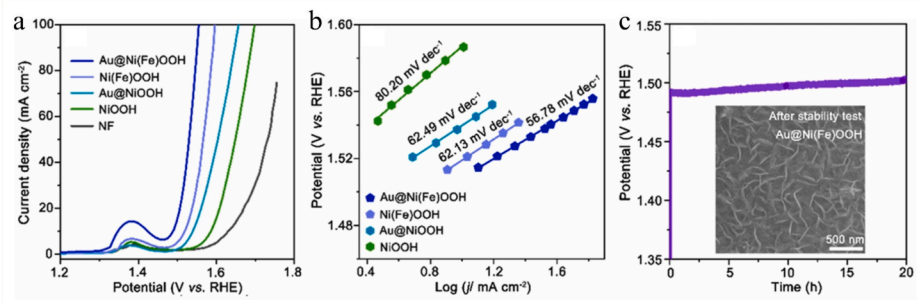

Fig. 9. (a) OER polarization curves and (b) Tafel slopes of NiOOH, Ni(Fe)OOH, Au@NiOOH and Au@Ni(Fe)OOH, (c) time-dependent potential variation curve of Au@Ni(Fe)OOH, inset in (c) is the SEM image of Au@Ni(Fe)OOH after the chronopotentiometry test. Reproduced with permission from ref [101].Copyright 2022 Elsevier.

Table 5
The OER catalytic performance of Au-driven non-noble metal oxyhydroxides.

Catalyst	Electrolyte	Overpotential (mV vs RHE)	Overpotential decrement (mV)	Tafel slope (mV/dec)	Ref
Au@NiFeOOH	1 mol/L KOH	258@10 mA cm^{-2}	31	56.78	[101]
NiFeOOH	1 mol/L KOH	289@10 mA cm^{-2}		62.13	
Au@NiOOH	1 mol/L KOH	308@10 mA cm^{-2}	46	62.49	
NiOOH	1 mol/L KOH	354@10 mA cm^{-2}		80.20	
Au/Cr-NiFeOOH	0.1 mol/L KOH	323@10 mA cm^{-2}		33	[102]
Au-NiFeOOH	0.1 mol/L KOH	350@10 mA cm^{-2}		37	
Au-NiCrOOH	0.1 mol/L KOH	600@10 mA cm^{-2}		157	
Au-FeCrOOH	0.1 mol/L KOH	460@10 mA cm^{-2}		39	

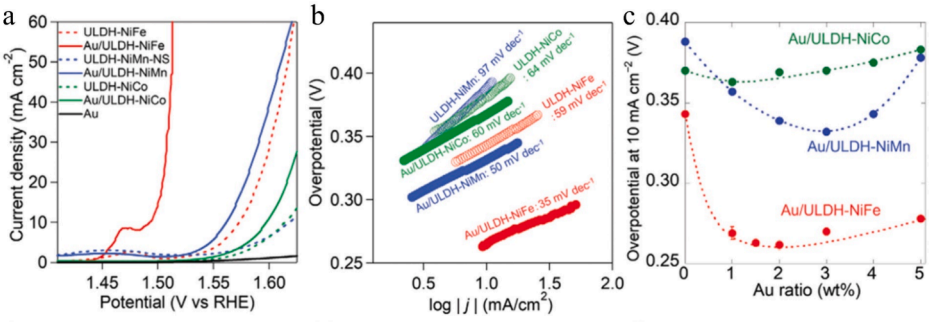

Fig. 10. (a) OER curves and (b) Tafel curves of Au/ULDH and ULDHs, (c) Overpotential at 10 mA cm^{-2} as a function of the loading amount of Au clusters. Reproduced with permission from ref [105]. Copyright 2022 John Wiley and Sons.

Table 6
The OER catalytic performance of Au-driven non-noble metal layered double hydroxides.

Catalyst	Electrolyte	Overpotential (mV vs RHE)	Overpotential decrement (mV)	Tafel slope (mV/dec)	Ref
AuNiFe-ULDH	1 mol/L KOH	262@10 mA cm^{-2}	81	35	[105]
NiFe-ULDH	1 mol/L KOH	343@10 mA cm^{-2}		59	
AuNiMn-ULDH	1 mol/L KOH	332@10 mA cm^{-2}	38	50	
NiMn-ULDH	1 mol/L KOH	370@10 mA cm^{-2}		97	
AuNiCo-ULDH	1 mol/L KOH	363@10 mA cm^{-2}	25	60	
NiCo-ULDH	1 mol/L KOH	388@10 mA cm^{-2}		64	
AuNiFe LDH	1 mol/L KOH	237@10 mA cm^{-2}	26	36	[104]
NiFe LDH	1 mol/L KOH	263@10 mA cm^{-2}		60	
AuNiFe LDH	1 mol/L KOH	270@500 mA cm^{-2}	44	48.4	[103]
NiFe LDH	1 mol/L KOH	314@500 mA cm^{-2}		71.1	
Au-CaFeMg LDH	1 mol/L KOH	450@Onset	500	68	[106]
CaFeMg LDH	1 mol/L KOH	950@Onset		242	
Au NPs	1 mol/L KOH	850@Onset		235	
Au-CuMgFe LDH	1 mol/L KOH	530@10 mA cm^{-2}	490	53	[107]
CuMgFe LDH	1 mol/L KOH	920@5mA cm^{-2}		294	
Au NPs	1 mol/L KOH	920@10 mA cm^{-2}		249	

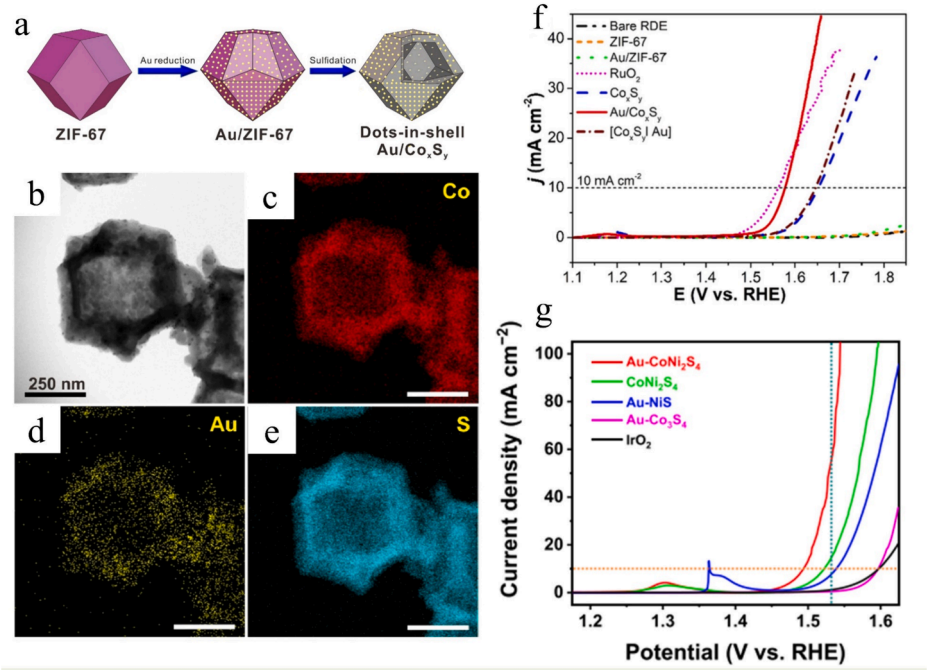

Fig. 11. (a) Synthesis diagram of Au/Co_xS_y, (b) TEM and (c-e) EDX element diagram of Au/Co_xS_y, (f) OER performance test of a variety of catalysts. Reproduced with permission from ref [108].Copyright 2022 Elsevier. (g) LSV curves for the Au–$CoNi_2S_4$core–shell NPs and other catalysts. Reproduced with permission from ref [111]. Copyright 2021 IOP Publishing.

Table 7
The OER catalytic performance statistics of Au-driven non-noble metal sulfides.

Catalyst	Electrolyte	Overpotential (mV vs RHE)	Tafel slope (mV/dec)	Overpotential decrease(mV)	Ref
Au/Co_xS_y	0.1 mol/L KOH	343@10 mA cm^{-2}	62	80	[108]
Co_xS_y	0.1 mol/L KOH	423@10 mA cm^{-2}	78		
AuCo_xS_y	0.1 mol/L KOH	345@10 mA cm^{-2}	138	73	[109]
Co_xS_y	0.1 mol/L KOH	418@10 mA cm^{-2}	145		
$AuNiCo_2S_4$	1 mol/L KOH	299@10 mA cm^{-2}	44.5	13	[110]
$NiCo_2S_4$	1 mol/L KOH	312@10 mA cm^{-2}	49.1		
$AuCoNi_2S_4$	1 mol/L KOH	264@10 mA cm^{-2}	35.6	28	[111]
$CoNi_2S_4$	1 mol/L KOH	292@10 mA cm^{-2}	50.2		
$AuNi_2S_4$	1 mol/L KOH	309@10 mA cm^{-2}	56.1		
$AuCo_3S_4$	1 mol/L KOH	366@10 mA cm^{-2}	59.7		
Au-$NiCoFe_7S_8$	1 mol/L KOH	243@10 mA cm^{-2}	43		[112]
Au-$NiFe_7S_8$	1 mol/L KOH	259@10 mA cm^{-2}	41		
Au-$CoFe_7S_8$	1 mol/L KOH	275@10 mA cm^{-2}	44		
Au-Fe_7S_8	1 mol/L KOH	370@10 mA cm^{-2}	73		
Au/Ni_3S_2/NF	1 mol/L KOH	230@10 mA cm^{-2}	51	73	[113]
Ni_3S_2/NF	1 mol/L KOH	303@10 mA cm^{-2}	111		

3.2.6. *Nitrides OER activity of Au-driven*

Lv et al prepared a nanocrystalline electrocatalyst (Fig. 13**a**) of Au modified Ni_3N by using co-precipitation and nitridation methods and the morphology of the catalyst was exhibited in Fig. 13**b**. HRTEM image (Fig. 13**c**) illustrated that Au NPs were uniformly dispersed on the surface of Ni_3N. The Au/Ni_3N exhibited an excellent OER activity as the Au loading of 2 wt% (marked as $AuNi_3N$-10) (Fig. 13**d**) and its durability was superior than the IrO_2 as well (Fig. 13**e**). Experimental results and theoretical calculations showed that Au NCs would effectively regulate the electronic structure of Ni_3N and reduce the energy barrier associated with OER activity [117].

Nguyen et al synthesized the core–shell Au@$Co_2N_{0.67}$ nanodots on N-doped graphene hollow microspheres (Au@$Co_2N_{0.67}$/3D-NGr), where the white core STEM image was the Au core, and the shell layer was determined as $Co_2N_{0.67}$. The overvoltage of the Au@$Co_2N_{0.67}$/3D-NGr was 280.5 mV at the current density of 10 mA cm^{-2} in 1 mol/L KOH, which is significantly superior to the $Co_2N_{0.67}$/3D-NGr (304.2 mV), and the Au@$Co_2N_{0.67}$/3D-NGr also exhibited excellent catalytic performance for HER and ORR [118]. Yao et al prepared a self-supporting flexible electrode of Au/$CoMoN_x$, where the OER catalytic activity of the Au/$CoMoN_x$ was apparently higher than the $CoMoN_x$, with a reduction of 140 mV on the overpotential at 10 mA cm^{-2} and a decrease of 23 mV dec^{-1} in the Tafel slope [119]. The OER activity of Au-driven non-noble metal nitrides was shown in Table 9.

3.2.7. *Selenides OER activity of Au-driven*

Zhao et al studied $CoSe_2$ nanoribbons modified with Au single atoms (Fig. 14**a**) and the HRTEM image (Fig. 14**b**) showed that the ordered interlayer distance was in the size of 1.0 nm. The HAADF-STEM analysis in Fig. 14**c** illustrated that the Au single atoms were uniformly distributed on the $CoSe_2$ matrix and the elemental atlas presented the distribution of Co, Se, and Au elements on the nanobelt in Fig. 14**d**. Electrochemical analysis showed that the $CoSe_2$ catalysts modified via Au single atoms owned the highest OER catalytic activity at 10 mA cm^{-2}

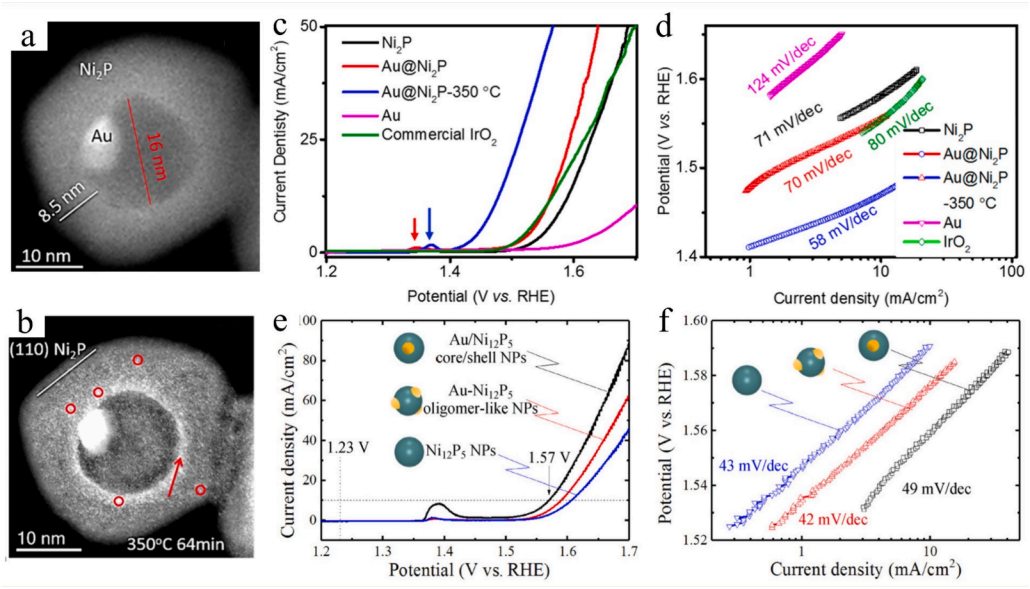

Fig. 12. (a) TEM images of fresh Au@Ni_2P, (b) TEM images of Au@Ni_2P after heating at 350 ℃ for 64 min, (c) OER catalyst performance and (d) Tafel plot before and after heating at 350 °C compared with other samples. Reproduced with permission from ref [114]. Copyright 2019 American Chemical Society. (e) OER test and (f) Tafel plots reported Au/$Ni_{12}P_5$ core/shell NPs, Au-$Ni_{12}P_5$ oligomer-like NPs and pure $Ni_{12}P_5$ NPs. Reproduced with permission from ref [115]. Copyright 2017 Springer Nature.

Table 8
The OER catalytic performance of Au-driven non-noble metal phosphide.

Catalyst	Electrolyte	Overpotential (mV vs RHE)	Tafel slope (mV/dec)	Overpotential decrease(mV)	Ref
Au@Co_2P	1 mol/L KOH	321@10 mA cm^{-2}	57	95	[116]
Co_2P	1 mol/L KOH	416@10 mA cm^{-2}	101		
Au@Ni_2P-350℃	1 mol/L KOH	336@50 mA cm^{-2}	58	121	[114]
Ni_2P	1 mol/L KOH	457@50 mA cm^{-2}	71		
Au@$Ni_{12}P_5$(core/shell)	1 mol/L KOH	340@10 mA cm^{-2}	49	40	[115]
Au@$Ni_{12}P_5$(oligomer/like)	1 mol/L KOH	360@10 mA cm^{-2}	42		
$Ni_{12}P_5$	1 mol/L KOH	380@10 mA cm^{-2}	43		

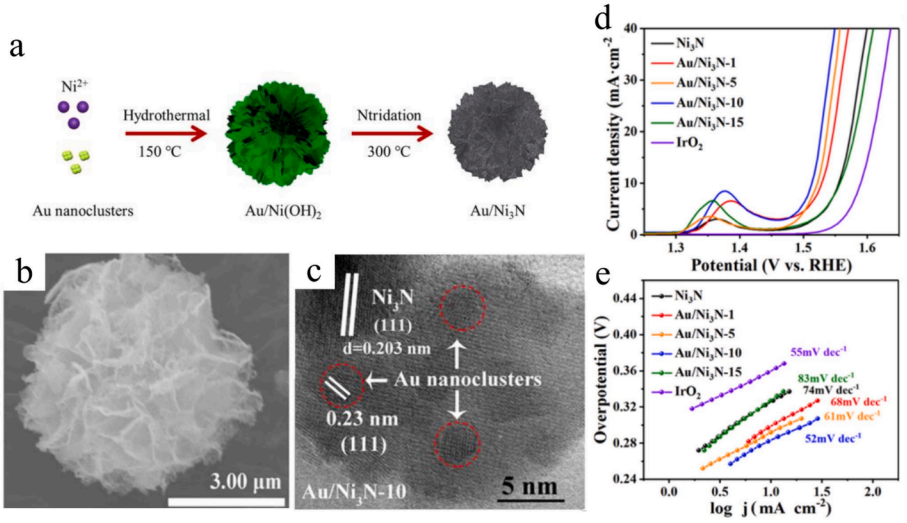

Fig. 13. (a) Illustration of prepared 3D microflowers structure Au/Ni_3N samples, (b) SEM images of Au/$Ni(OH)_2$, (c) TEM images of Au/Ni_3N (red circular lines indicate surface distribution of Au), (d) OER test of Au/Ni_3N and others, (e) Tafel slope of Au/Ni_3N and others. Reproduced with permission from ref [117]. Copyright 2019 John Wiley and Sons. (For interpretation of the references to colour in this figure legend, the reader is referred to the web version of this article.)

Table 9
The OER catalytic performance of Au-driven non-noble metal nitride.

Catalyst	Electrolyte	Overpotential (mV vs RHE)	Tafel slope (mV/dec)	Overpotential decrease(mV)	Ref
$AuNi_3N$	0.1 mol/L KOH	280@10 mA cm^{-2}	52	40	[117]
Ni_3N	0.1 mol/L KOH	320@10 mA cm^{-2}	74		
IrO_2	0.1 mol/L KOH	360@10 mA cm^{-2}	55		
$AuCoMoN_4$	1 mol/L KOH	230@10 mA cm^{-2}	46	140	[119]
$AuCoN_4$	1 mol/L KOH	310@10 mA cm^{-2}	68		
$AuRuO_2$	1 mol/L KOH	311@10 mA cm^{-2}	47		
$CoMoN_4$	1 mol/L KOH	370@10 mA cm^{-2}	69		
$Au@Co_2N_{0.67}$/3D-NGr	1 mol/L KOH	280.5@10 mA cm^{-2}	56.5	23.7	[118]
$Co_2N_{0.67}$/3D-NGr	1 mol/L KOH	304.2@10 mA cm^{-2}	65		

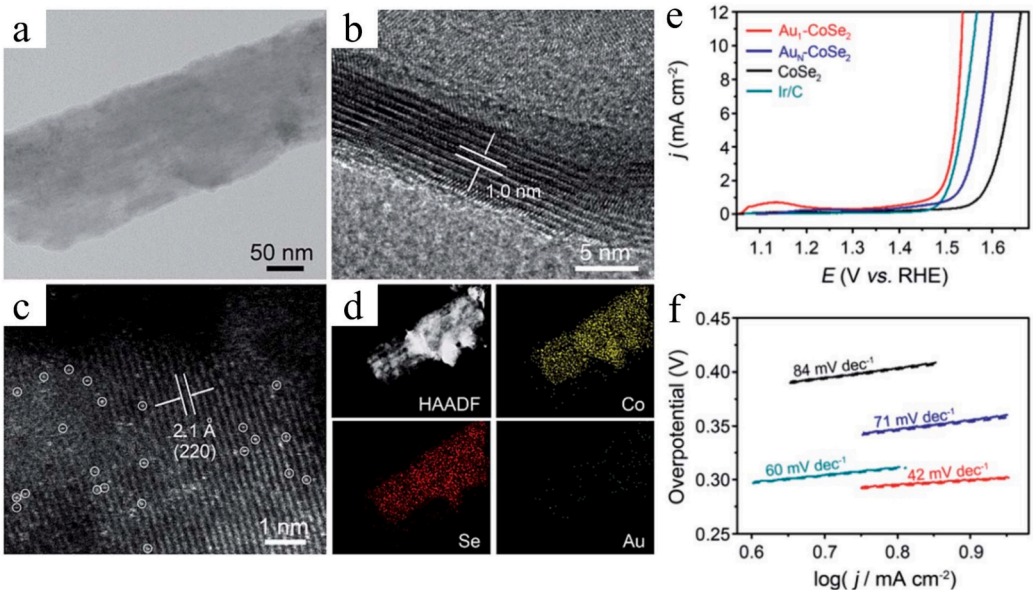

Fig. 14. (a) TEM and (b) HRTEM of Au_1–$CoSe_2$ nanobelts, (c) HAADF-STEM Isolated Au atoms marked by white circles are uniformly dispersed on the nanobelts, (d) STEM-EDX element map of Co, Se, and Au in Au_1–$CoSe_2$ nanobelts, (e) OER test of Au_1–$CoSe_2$, Au_NCoSe_2 and others, (f) Tafel curve of Au_1–$CoSe_2$, Au_NCoSe_2 and others. Reproduced with permission from ref [120]. Copyright 2017 The Royal Society of Chemistry.

in Fig. 14**e**, where the current density of the Au_1-$CoSe_2$ at the overvoltage of 300 mV was 21.1, 5.7 and 1.9 times of the $CoSe_2$, Au_N-$CoSe_2$ (Au NP-deposited $CoSe_2$ nanobelts)and Ir/C catalysts, respectively. Fig. 14**f** depicted that the Tafel slope of the Au_1-$CoSe_2$ was just 42 mV dec^{-1}, which was much lower than the $CoSe_2$, AuN-$CoSe_2$, and Ir/C catalysts, and the stability of the Au_1-$CoSe_2$ was also the best. All these data further confirmed that Au single atom possessed strong strengthening effect [120]. The OER catalytic performance of Au-driven non-noble metal selenides was shown in Table 10.

Table 10
OER catalytic performance statistics of Au-driven non-noble-metal selenides.

Catalyst	Electrolyte	Overpotential (mV vs RHE)	Overpotential decrement (mV)	Tafel slope (mV/dec)	Ref
Au_1CoSe_2	0.1 mol/L KOH	303@10 mA cm^{-2}	120	42	[120]
Au_NCoSe_2	0.1 mol/L KOH	375@10 mA cm^{-2}		71	
$CoSe_2$	0.1 mol/L KOH	423@10 mA cm^{-2}		84	
$Au_{25}CoSe_2$	0.1 mol/L KOH	430@10 mA cm^{-2}	90	–	[121]
$CoSe_2$	0.1 mol/L KOH	520@10 mA cm^{-2}		–	

4. Mechanisms of Au-driven oxygen evolution electrocatalysis

In general, the OER is crucial for both water-splitting and metal-air batteries in aqueous electrolytes. It can be categorized into two mechanisms: namely AEM (adsorption evolution mechanism) and LOM (lattice oxygen mediated mechanism), based on the active sites involved. The process of OER in both alkaline and non-alkaline environments can be represented as follows:[122]

$$4OH^- \rightarrow O_2 + H_2O + 4e^- (\text{alkaline media}) \quad (1)$$

$$2H_2O \rightarrow O_2 + 4H^+ + 4e^- (\text{non} - \text{alkaline media}) \quad (2)$$

Au is known as showing the best electronegativity among all metal elements, which is derived from the strong covalent bond formed between Au and oxygen (O) in the Au-O bond. The energy band of the Au-O bond is primarily made up of oxygen *p* orbitals. Additionally, the electronic structure of the catalyst and interact with oxygen vacancies can be modified by Au. In this section, we will discuss how metallic Au contributes to the improvement of the catalytic activity for the OER and explain the underlying mechanism.

4.1. AEM mechanism

In the AEM mechanism, metal is regarded as the redox center. Fig. 15 shows the OER process in alkaline and non-alkaline media following the AEM mechanism. The reaction path in an alkaline solution could be

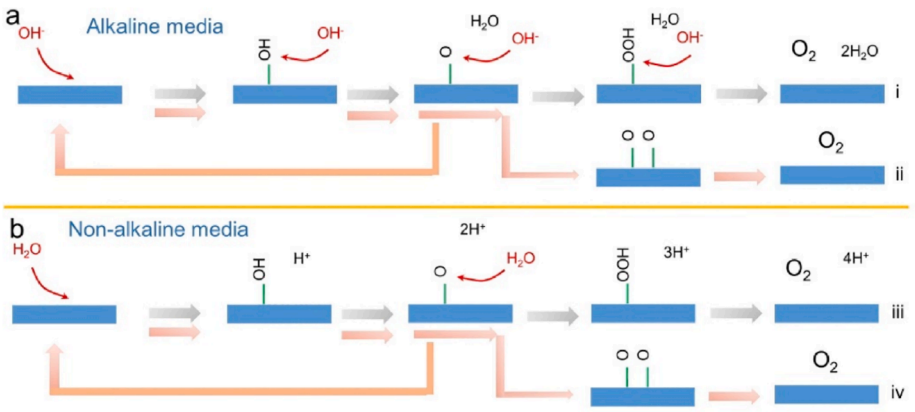

Fig. 15. AEM mechanism of OER in alkaline (a) and non-alkaline media (b), chemicals marked in red mean that they are provided by media. Reproduced with permission from ref [122]. Copyright 2022 Elsevier. (For interpretation of the references to colour in this figure legend, the reader is referred to the web version of this article.)

described as following:

$$M + OH^- \rightarrow MOH + e^- \quad (3)$$

$$MOH + OH^- \rightarrow MO + H_2O + e^- \quad (4)$$

$$MO + OH^- \rightarrow MOOH + e^- \quad (5)$$

$$MOOH + OH^- \rightarrow M + O_2 + H_2O + e^- \quad (6)$$

$$2MO \rightarrow 2M + O_2(g) \quad (7)$$

The reaction path in non-alkaline:

$$M + H_2O \rightarrow MOH + H^+ + e^- \quad (8)$$

$$MOH \rightarrow MO + H^+ + e^- \quad (9)$$

$$MO + H_2O \rightarrow MOOH + H^+ + e^- \quad (10)$$

$$MOOH \rightarrow M + O_2 + H^+ + e^- \quad (11)$$

$$2MO \rightarrow 2M + O_2(g) \quad (12)$$

For the AEM mechanism, the surface of catalyst is considered as a stable platform and only the valence state of the catalytic center (metal site) changes during the release of oxygen intermediates. If the reaction mechanism of OER can be changed, the scaling relationship of the AEM mechanism (Fig. 16**a**) can be avoided, and the performance of OER will be greatly improved, that is, the direct O-O coupling (DOOC) occurs as displayed in Fig. 16**b**. The adsorption of Au element on oxygen is weak. The Fermi energy level of the Au-O bond-related energy band is mainly composed of oxygen *p* orbitals. If *O intermediates can be formed on the Au cluster, the Au cluster can be used as the active site of the DOOC mechanism. However, due to its poor adsorption of oxygen-containing intermediates, the OER activity of Au itself is very low [105].

Kitano et al studied the single-layer-stripped layer-like hydrogen oxide (ULDH) electrocatalyst of the Au nanomole cluster [105]. The combination of Au NCs and ULDH (with extremely high surface area per unit volume) will produce interfacial active sites between Au NCs and ULDH. These interfacial active sites could initiate dehydrogenation on ULDH and form O* intermediates on Au. Direct O-O coupling (interface-DOOC) occurred at the heterogeneous interface between the Au cluster and the ULDH active site. The detailed mechanism was shown in Fig. 16**c** ~ **16d**, which has significantly improved OER performance.

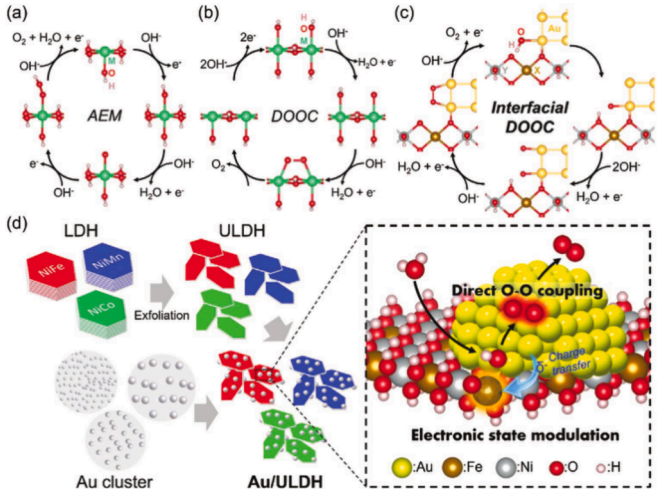

Fig. 16. (a) AEM, (b) DOOC, and (c) interfacial DOOC of OER pathway, (d) the synthesis process of Au/ULDH catalyst and the concept of interface active sites between Au cluster and ULDH to enhance OER activity. Reproduced with permission from ref [105]. Copyright 2022 John Wiley and Sons.

4.2. LOM mechanism

In the context of solid oxide/(oxygen) hydroxide electrocatalyst series, the OER process involves the participation of lattice oxygen. In the LOM pathway, the catalytic surface undergoes dynamic changes during the release of oxygen, rendering it thermodynamically unstable. The process of OER involves the oxidation, exchange, and release of oxygen ligands on the surface lattice of the catalyst. OH^-/H_2O combines with oxygen vacancy to form a new "lattice oxygen" for the subsequent cycle. Hence, the successful triggering of the LOM pathway necessitates the activation of lattice oxygen, which relies on the unique electronic structure of the catalyst body, particularly the lattice oxygen itself. Based on this fundamental principle of LOM, several OER pathways with distinct active centers have recently been proposed (Fig. 17**a–c**) [123].

Considering the aforehand activation of lattice oxygen, the activated lattice oxygen can readily act as an active site. The lattice oxygen directly adsorbed OH^- and forms *OOH species by nucleophilic attack. The release of gaseous O_2 generates an oxygen vacancy, which is refilled by OH^-, and is therefore called oxygen vacancy site mechanism (OVSM, Fig. 17**a**) [124]. The other mechanism is that still a single metal site (SMSM, Fig. 17**b**) acting as the catalytic center adsorbs OH^- and then the surface reconstruction makes the *O intermediate directly coupled with the activated lattice oxygen. The *OO species can be transformed into an O_2 molecule [125]. In addition to a single active center, it is also speculated that there is a bimetallic site mechanism (DMSM, Fig. 17**c**) [126]. The intramolecular oxygen coupling of adjacent activated lattice oxygen

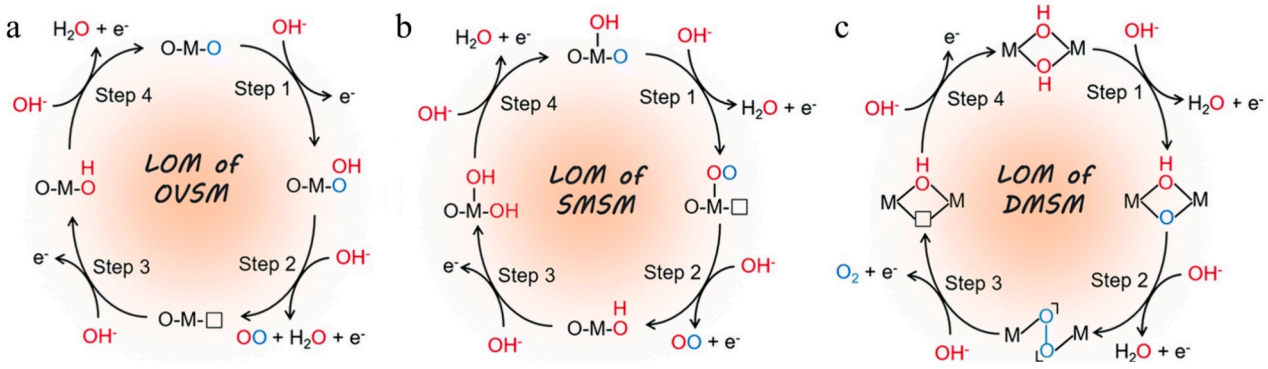

Fig. 17. (a) Oxygen vacancy site mechanism (OVSM), (b) single metal site mechanism (SMSM), and (c) dual-metal-site mechanism (DMSM). Chemical inert lattice oxygen, OER active lattice oxygen, and oxygen from the electrolyte are marked with black, blue, and red respectively. Reproduced with permission from ref [123]. Copyright 2021 Royal Society of Chemistry. (For interpretation of the references to colour in this figure legend, the reader is referred to the web version of this article.)

is expected to form M−OO−M, in which the formed *OO* moiety typically acts as a peroxygen-like species.

With the study of the LOM oxygen precipitation mechanism based on lattice oxygen, some studies have found that there existed a synergistic effect between lattice oxygen and Au. Cai et al studied the OER activity of single-atom Au-doped Co-based nanosheets theoretically and experimentally, and the overpotentials at 10 mA cm^{-2} were found in the sequence of α-$Co(OH)_2$ < Co_3O_4 < CoOOH < Au-$Co(OH)_2$. The calculation showed that the theoretical overpotentials (|ΔGmax-1.23|) under the AEM mechanism (Fig. 18**a, b**) had no significant change, where Co $(OH)_2$ was 1.07 eV, and Au-$Co(OH)_2$ was 1.11 eV, inconsistent with the experimental results. The simulation indicates that the center of the *d* band of Au-$Co(OH)_2$ configuration shifts to the right (Fig. 18**c**), which increases the non-bonding state of oxygen (Fig. 18**d**) and enhances the adsorption of oxygen intermediates. According to the calculation of the LOM mechanism (Fig. 18**e, f**), the overvoltage decreased from 1.07 eV to 0.78 eV, indicating that Au enhanced the activity of oxygen vacancies and promoted the direct formation of O-O bonds by the LOM mechanism, thus providing high OER activity [94].

Zhang et al carried out a detailed analysis of the effect of oxygen vacancies and Au in hematite on the OER catalytic performance. With the increase of oxygen vacancy (V_o) coverage, the *d*-band orbital of Fe atoms moves to the right (Fig. 19**c**), the center of the *d*-band increases, the anti-bond orbital filling of oxygen atom decreases, and the adsorption of oxygen gradually increases (Fig. 19**a**). The theoretical overpotential of OER decreased firstly and then increased with the coverage

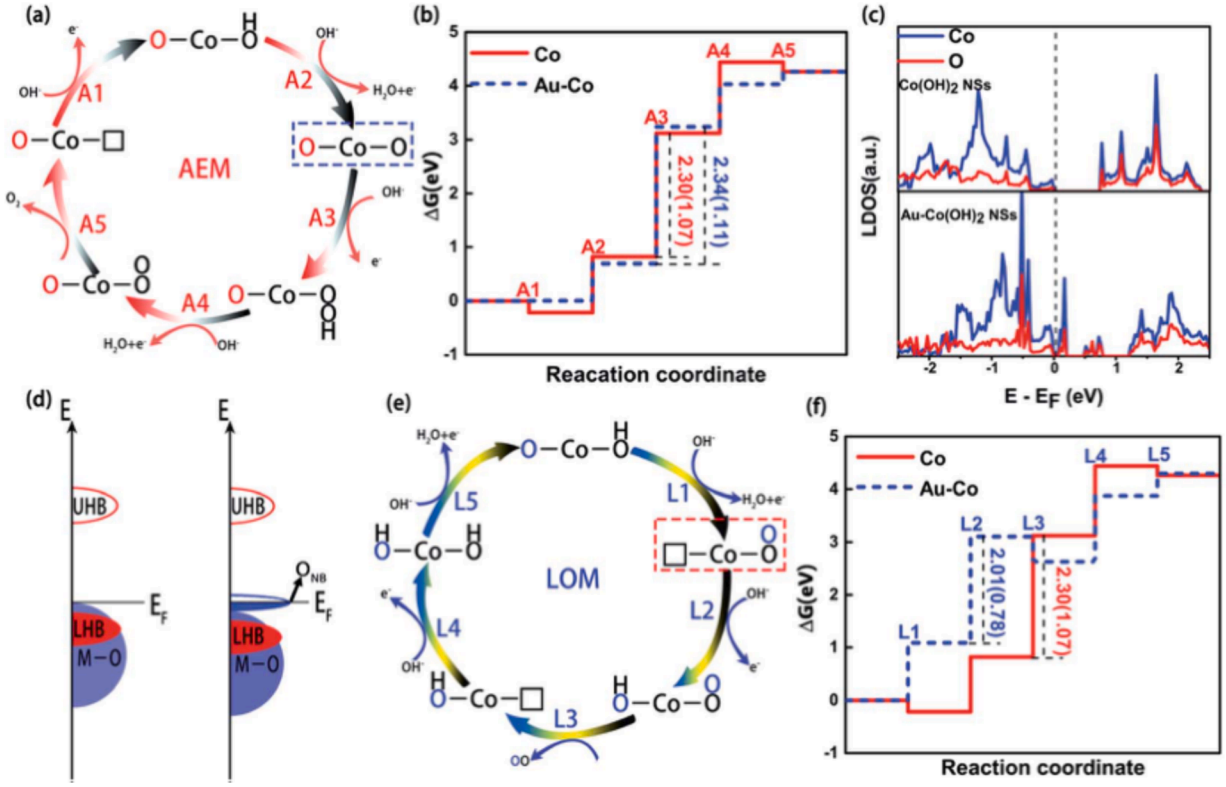

Fig. 18. (a) OER reaction pathway of Au-$Co(OH)_2$ in AEM, (b) the free energy distribution of Au-$Co(OH)_2$ (expressed as Au-Co) and $Co(OH)_2$ (expressed as Co) in the AEM reaction stage in AEM, (c) the DOS of $Co(OH)_2$ and Au- $Co(OH)_2$, (d) the energy band diagram of Au-$Co(OH)_2$ and $Co(OH)_2$, the oxygen non-bonding state (O_{NB}) above the Fermi level of Au-$Co(OH)_2$, (e) OER reaction pathway in LOM mechanism, (f) free energy distribution of Au-$Co(OH)_2$ and $Co(OH)_2$ in LOM reaction stage. Reproduced with permission from ref [94]. Copyright 2022 Royal Society of Chemistry.

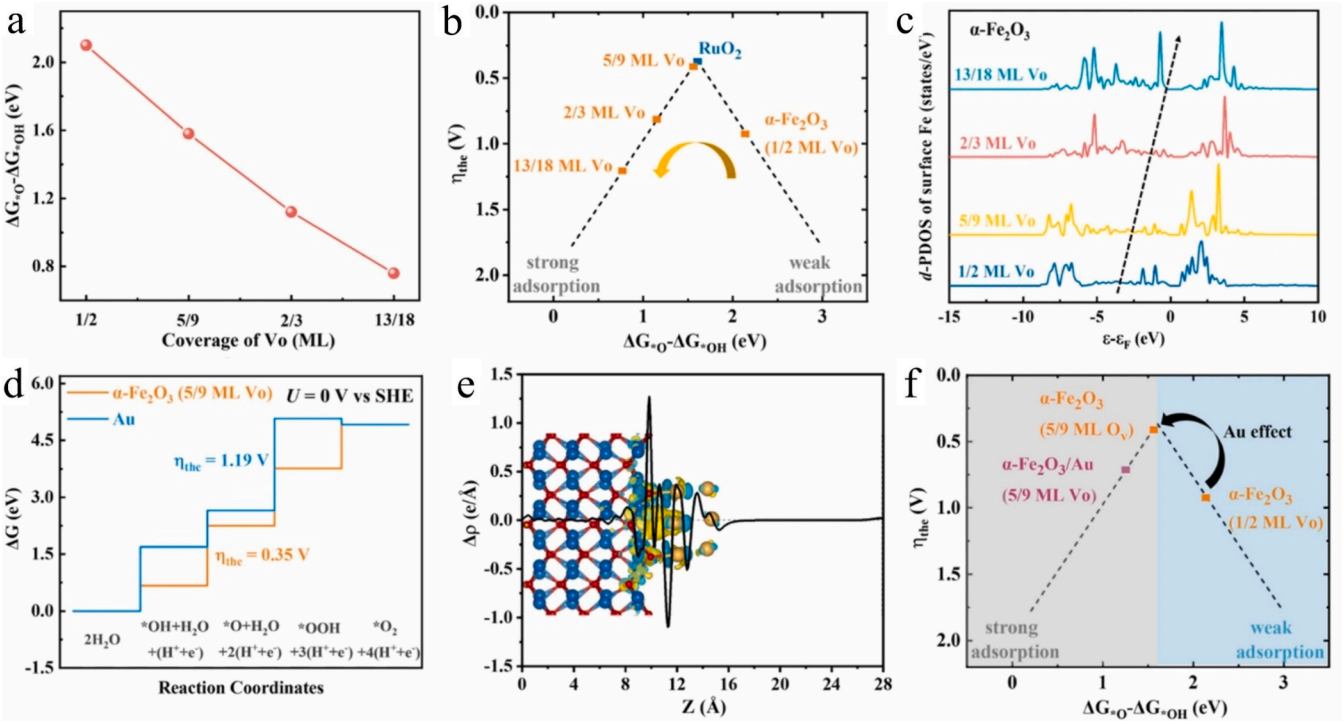

Fig. 19. (a) The change trends of the (ΔG_{*O}-ΔG_{*OH}) value with Vo coverages, (b) theoretical overpotential with different coverages of oxygen vacancy, (c) d-orbital density of states of iron atoms under different Vo coverage, (d) OER standard free energy diagram on α-Fe_2O_3 (1 1 0) with 5/9 ML Vo and Au (1 1 1) surfaces, (e) the one-dimensional differential electron density diagram of α-Fe_2O_3/Au (yellow represents electron aggregation, cyan represents electron dissipation), (f) the influence mechanism of Au on the OER activity of α-Fe_2O_3. Reproduced with permission from ref [127]. Copyright 2022 Elsevier. (For interpretation of the references to colour in this figure legend, the reader is referred to the web version of this article.)

of V_o (Fig. 19**b**). The electrons of Au transfer to Fe_2O_3 (Fig. 19**e**), which enhances the adsorption ability of oxygen. The excellent OER catalytic performance of α-Fe_2O_3/Au can be explained by the synergistic effect of Au and V_o (Fig. 19**d, f**) [127].

Liu et al conducted experimental studies on the modification of NiFe hydroxyl oxide by Au NPs. The possible mechanism surface-active sites (Fig. 20**a**) of Au@Ni(Fe)OOH are calculated as shown in Fig. 20**b**. It could be found that Fe on the surface of Au@Ni(Fe)OOH is regarded as the main active center. The overvoltage of Fe + V_o is 0.67 eV, which is significantly higher than 1.02 eV and 0.85 eV of V_o and Ni + V_o. The addition of Au affects the electronic structure near the interface, enhances the oxygen adsorption ability of Ni + V_o, Fe + V_o sites, and the overpotentials to 0.98 eV and 1.21 eV respectively, while the overpotential of Au at the interface decreases to 0.47 eV. Therefore, Au at the interface was proven the main active site. Fig. 20**c** shows the linear proportional relationship between ΔG(OOH) and ΔG(O) of the active

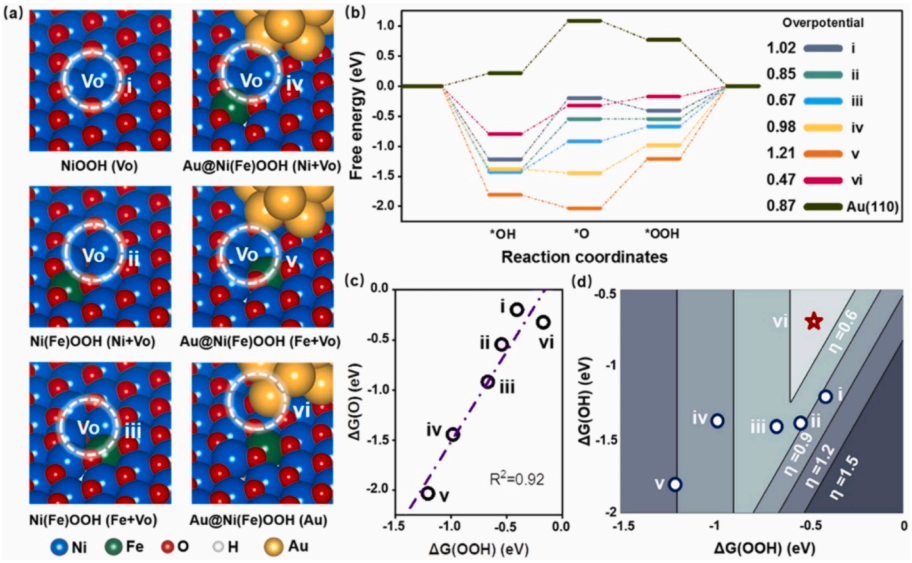

Fig. 20. (a) (i–vi) Structural models of all possible active sites of Au@Ni(Fe)OOH, (b) calculated free energy diagram for OER of all possible active sites of Au@Ni(Fe)OOH, (c) the linear proportional relationship between ΔG(OOH) and ΔG(O), (d) two-dimensional activity volcano plot with the optimal region (shown in bright) based on the thermodynamic results on the six considered active sites. Reproduced with permission from ref [101]. Copyright 2022 Elsevier.

site and its adsorption of oxygen conforms to the linear proportional relationship. Fig. 20**d** is a two-dimensional volcanic map of active sites. The binding of Au NPs sites adjacent to Fe + V_o and Ni + V_o with intermediates is significantly stronger than other sites appearing in the lower left corner. The interface of Au site in Au@Ni(Fe)OOH is in the intermediate, which is neither too strong nor weak and has a minimum overvoltage of 0.47 eV [101].

4.3. Identification of the real active sites

Many OER electrocatalysts experienced dynamic and irreversible reconstruction processes during the electrocatalytic reaction process. The transition metal oxyhydroxides were a true catalytic species formed during the reconstruction process typically expressed high OER activity. The proposed reconstruction causations are classified into four categories (Fig. 21): 1) lattice oxygen evolution-induced reconstruction; 2) metal leaching induced reconstruction; 3) preoxidation of anion species; 4) Ligand substitution [128].

In the OER oxidizing environment, the H on the outermost surface of NiFe LDH will detach from LDH to form NiFe oxyhydroxide. Zhang et al loaded 0.4 wt% single atom Au on NiFe LDH, and successfully increased the OER catalytic activity (Fig. 22**a**). Situ Raman spectroscopy was performed during CV (from 1.12 to 1.44 V to 1.12 V) scanning to characterize the structural transition of Au/NiFe LDH (Fig. 22**b**). The Ni-O vibrational peaks of LDH nanocrystals were observed at 462 cm^{-1} and 535 cm^{-1} in the range of 1.12 V to 1.32 V. When the potential was scanned to 1.44 V, new peaks appeared at 475 cm^{-1} and 559 cm^{-1}, which is the characteristic peak of NiOOH, indicating that LDH has been converted to NiFe oxyhydroxide. When the voltage was scanned again to 1.12 V the peak remained unchanged. The conversion of NiFe LDH to NiFe oxyhydroxide in the OER reaction is irreversible. Further analysis was also conducted on the effect of Au on the surface of NiFe LDH (Fig. 22**c**). The calculation and analysis results showed that Au injected a net charge of 0.32 e into the LDH and then into the surrounding O, Ni, and Fe atoms. Finally, this transferring process results in changing the local environment of the reaction site, which is more conducive to the adsorption of OH^- on the surface, and reducing the energy barrier from the rate-controlled step O * to OOH *, improving the OER activity of the catalyst [104].

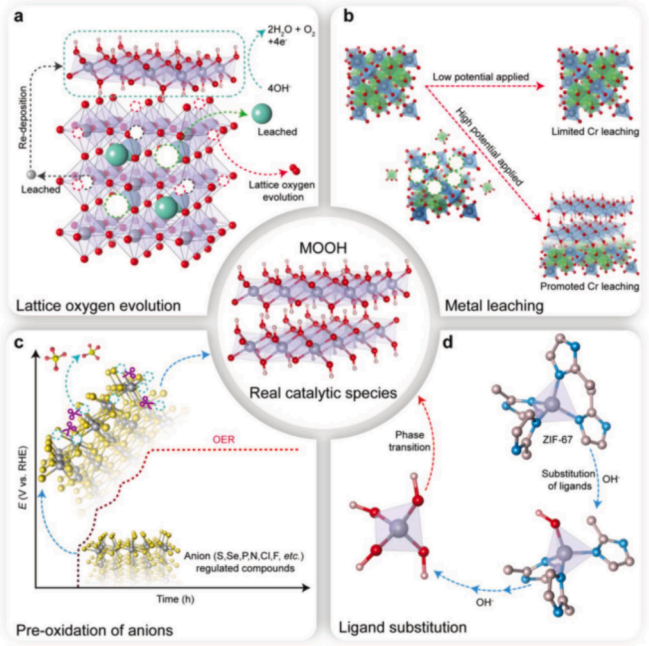

Fig. 21. Schematic illustrations of structural reconstruction mechanisms during OER. (a) Lattice oxygen evolution-induced reconstruction, (b) metal leaching induced reconstruction, (c) pre-oxidation of anions induced reconstruction, (d) ligand substitution by OH-induced reconstruction. Reproduced with permission from ref [128]. Copyright 2023 John Wiley and Sons.

The OER reaction intermediates can be characterized using in situ Raman spectroscopy. Cheng et al investigated the OER process of Fe, Co, and Ni metal–organic frameworks modified with nano Au ($Au_{5.30}$/(FCN) MOF/NP) using in situ Raman spectroscopy. Fig. 22**d and 22e** show that the two Raman peaks located at 476 cm^{-1} and 556 cm^{-1} apparently with increasing overpotential. These two bands are attributed to the bending vibration of M−O in MOOH and the tensile vibration of A_{1g}. The intensity ratio of the two characteristic peaks I_{476}/I_{556} is well agreed with OER activity. Fig. 22**f** shows that the strength ratio of $Au_{5.30}$/(FCN) MOF/NP, which is usually lower than that of (FCN) MOF/NP and OER activity gradually increases with increasing overpotential [78].

5. Multifunctional catalyst of Au-driven

Researchers have found that Au not only improves the OER performance of the catalyst but also plays an positive role in HER and ORR performance.

5.1. OER/HER bifunctional catalyst of Au-driven

Kwon et al investigated the OER/HER catalytic performance of AuRu alloy nanofibers. From the TEM in Fig. 23**a**, Au and Ru elements are uniformly distributed throughout the nanofiber, and no segregation phase is observed. It is also noticed that the interplanar spacing of Ru extended. The OER/HER catalytic activity (Fig. 23**b-c**) was evaluated in 0.5 M H_2SO_4, and the OER/HER catalytic activity of Ru was enhanced by Au. The OER test showed the lowest overpotential and Tafel slope at 10 mA cm^{-2}. The HER performance of AuRu alloy nanofibers was better than that of Ru/C. Some evidence proved that Au/Ru alloying accelerated the electrical activity and stability of the catalyst [75].

Liu et al studied Ni_3S_2 nanosheets modified with Au NPs and found that there is strong electron coupling at the interface by X-ray absorption fine structure (XAFS) and DFT calculations. Au NPs regulate the electronic structure of Ni_3S_2 and optimize the adsorption-free energy of intermediates. Fig. 23**d** shows that the Ni-S bond length in Au/Ni_3S_2 is 1.73, which is shorter than Ni_3S_2(1.78). The OER/HER catalytic activity (Fig. 23**e-f**) was tested in 1 M KOH. The OER activity of Au/Ni_3S_2/NF (230 mV@10 mA cm^{-2}) is better than that of Ni_3S_2/NF (303 mV@10 mA cm^{-2}). The HER activity of Au/Ni_3S_2/NF (97 mV@10 mA cm^{-2}) is better than that of Ni_3S_2/NF (149 mV@10 mA cm^{-2}). Au NPs enhance the OER/HER catalytic performance of Ni_3S_2 [113].

5.2. OER/ORR/HER trifunctional catalysts of Au-driven

Nguyen et al construction of Au@$Co_2N_{0.67}$ core–shell nanodots-interspersed 3D interconnected N-graphene hollow sphere network for ORR/OER/HER three functional catalysts. XPS analysis revealed that due to the high electronegativity of Au, Au forms electron-rich Au and electron-poor Co atoms were both formed. This electron-poor Co species is the main active site for catalysis. The ORR test and Tafel curve in 0.1 M KOH and the OER/HER test and corresponding Tafel in 1 M KOH are shown in Fig. 24**a-b, c-f**. The ORR/OER/HER catalytic activity of Au nanoparticles for $Co_2N_{0.67}$ was improved, the Tafel slope was reduced, the reaction kinetics were accelerated, and the stability of the catalyst was also promoted [118].

The slow kinetics of ORR and OER processes seriously limited its practical application of zinc-air battery. Nguyen et al synthesized a core–shell Au@$Co_2N_{0.67}$ catalyst, which exhibited good catalytic activity for ORR and OER. When it was applied to a zinc-air battery as shown in Fig. 24**g-h**, the battery performance was superior to conventional of Pt/C and RuO_2/C [118]. Luo et al synthesized AuPt nanoparticles supported on multi-walled carbon nanotubes (Au_xPt/MWNTs) catalysts for

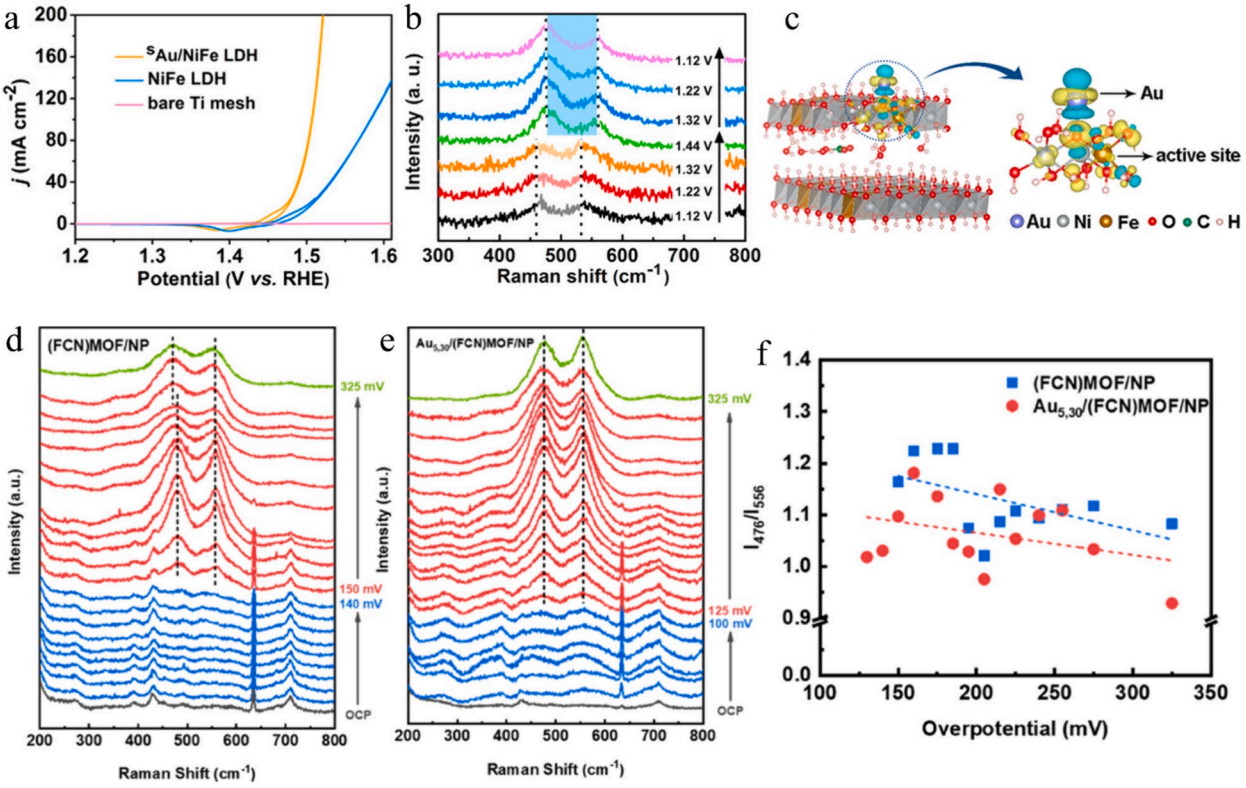

Fig. 22. (a) OER test of Au/NiFe LDH and other catalysts in 1 M KOH, (b) Raman spectra of Au/NiFe LDH at different potentials, (c) differential charge densities of NiFe LDH with and without Au atom when one O atom is adsorbed on the Fe site. The *iso*-surface value is 0.004 eÅ^{-3}. Yellow and blue contours represent electron accumulation and depletion, respectively. Reproduced with permission from ref [104].Copyright 2018 American Chemical Society. In-situ Raman spectra of (d) (FCN)MOF/NP and (e) $Au_{5.30}$/(FCN)MOF/NP at increasing applied potentials from OCP to overpotential of 325 mV, (f) peak intensity ratio of I_{476}/I_{566} for (FCN) MOF/NP and $Au_{5.30}$/(FCN)MOF/NP at increasing applied potentials from OCP to overpotential of 325 mV, with linearly fitted dash lines to show trend of data. Reproduced with permission from ref [78]. Copyright 2021 Elsevier. (For interpretation of the references to colour in this figure legend, the reader is referred to the web version of this article.)

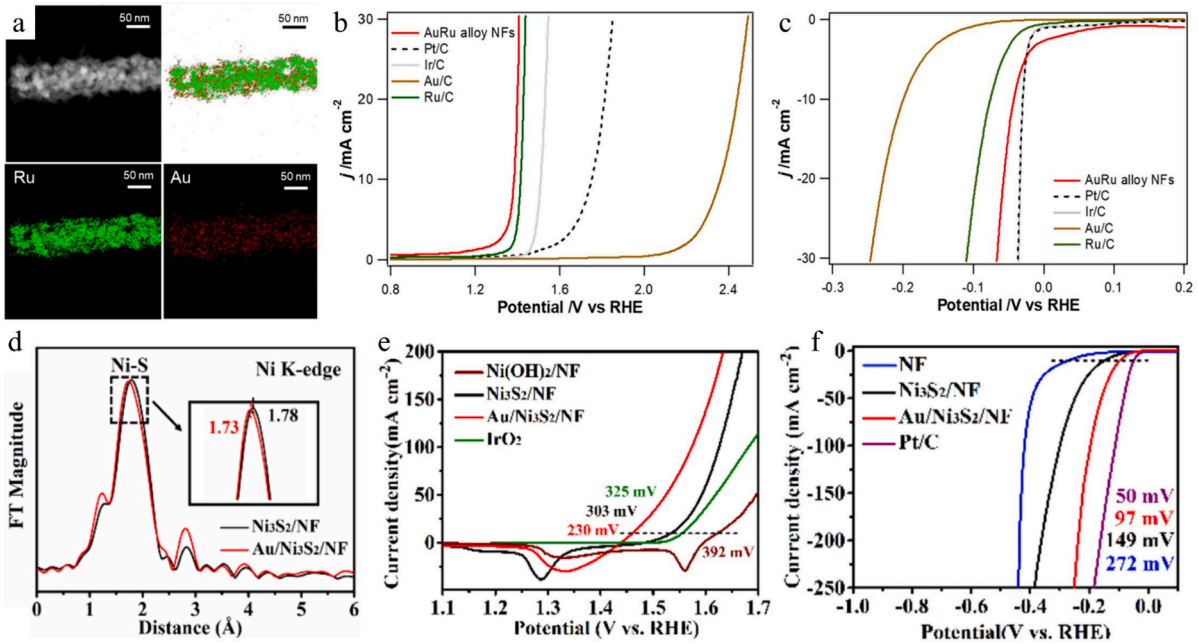

Fig. 23. (a) TEM of AuRu alloy NFs, (b) OER test and (c) HER test of AuRu alloy NFs Pt/C, Ir/C, Au/C, Ru/C in Ar-saturated 0.5 M H_2SO_4 aqueous solution. Reproduced with permission from ref [75]. Copyright 2021 Elsevier. (d) The Fourier transform k^3-weighted EXAFS spectra of Ni_3S_2/NF and Au/Ni_3S_2/NF, (e) OER test and (f) HER test of NF, Ni_3S_2/NF, Au/Ni_3S_2/NF, Pt/C. Reproduced with permission from ref [113]. Copyright 2022 Elsevier.

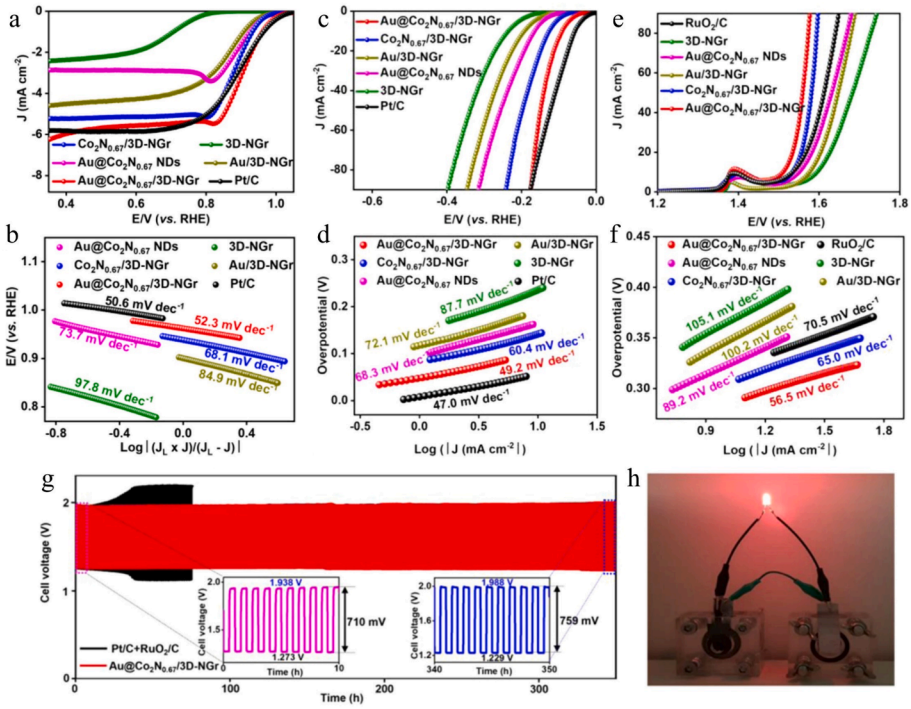

Fig. 24. (a) ORR test and corresponding Tafel curve (b), (c) HER test and corresponding Tafel curve (d), (e) OER test and corresponding Tafel curve (f) of $Au@Co_2N_{0.67}$/3D-NGr and others. Reproduced with permission from ref [118]. Copyright 2021 Elsevier. $Au@Co_2N_{0.67}$/3D-NGr water zinc air battery test, (g) charge–discharge cycle test of zinc-air battery, and (h) physical diagram of zinc-air battery lighting. Reproduced with permission from ref [118]. Copyright 2021 Elsevier.

an Al-air battery. The experimental results showed that the performance of Al-air battery with $Au_{1.68}Pt$/MWNTs (Au 8.95 wt%, Pt 5.3 wt%) was compared to that of 20 wt% Pt/C in terms of open circuit voltage, energy density, power density and stability. Consequently, the incorporation of Au and Pt NPs enhances the performance of Al air batteries [10].

6. Applications of Au-driven oxygen evolution electrocatalysis

Hydrogen energy is widely recognized as a viable alternative to fossil fuels. Electrochemical water splitting offers a dependable and eco-friendly approach to producing hydrogen. To enhance the efficiency of this process, it is crucial to develop a dual-purpose catalyst capable of promoting both the cathodic HER and the anodic OER during water splitting. Liu et al constructed Au/Ni_3S_2 heterostructure on foam nickel substrate and showed good OER (230 mV@10 mA cm^{-2}) and HER (97 mV@10 mA cm^{-2}) catalytic activity. As shown in Fig. 25**a**, water splitting in 1 M KOH only requires 1.52 V to provide 10 mA cm^{-2} current by using the dual-function catalyst [113]. Nguyen et al prepared an $Au@Co_2N_{0.67}$ core–shell catalyst with considerable catalytic activity for HER and OER. As shown in Fig. 25**b**, the electrolysis only needs 1.58 V to provide 10 mA cm^{-2} current with the dual-function catalyst in 1 M KOH [118]. Wang et al prepared a core–shell $Au@AuIr_2$ nanocatalyst as shown in Fig. 25**c**, which only needs 1.55 V to provide 10 mA cm^{-2} current for water splitting in 0.5 M H_2SO_4 solution [73]. Kwon et al synthesized AuRu nanofibers with excellent HER and OER catalytic activity in 0.5 M H_2SO_4 solution. As shown in Fig. 25**d**, only 1.438 V is needed to provide a 10 mA cm^{-2} current for water splitting [75].

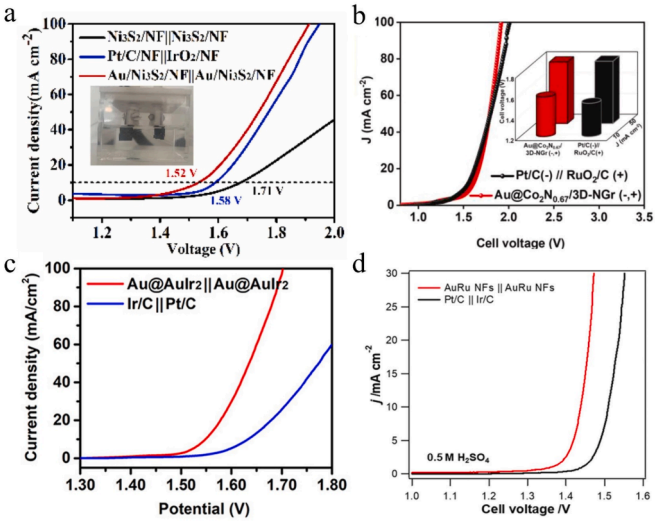

Fig. 25. (a) Two-electrode cell using Au/Ni_3S_2/NF as anode and cathode for water splitting in 1 M KOH. Reproduced with permission from ref [113]. Copyright 2022 Elsevier. (b) Two-electrode cell using $Au@Co_2N_{0.67}$/3D-NGr-coated NF as anode and cathode for water splitting in 1 M KOH, inset of (b) comparison of cell voltages at 10 and 50 mA cm^{-2}. Reproduced with permission from ref [118]. Copyright 2021 Elsevier. (c) Overall water splitting performance of $Au@AuIr_2$ in 0.5 M H_2SO_4. Reproduced with permission from ref [73]. Copyright 2021 American Chemical Society. (d) Overall water splitting performance of AuRu NFs in 0.5 M H_2SO_4. Reproduced with permission from ref [75]. Copyright 2021 Elsevier.

7. Conclusions

The commercial catalyst in industrial aspect is usually occupied by Pt-based catalyst, however, Au-based catalyst still has its own great development space. The transformation of bulk Au into nanosized Au leads to a shift from continuous to discrete in electronic spectra, resulting in the convergence of the HOMO of nanosized Au. This enables efficient electron transfer to oxygen and strengthens electrocatalytic performance. As the size decreasing of Au, the catalytic activity increases gradually. Au nanoparticles and Au nanoclusters exhibited

favorable ORR activity and limited OER activity. In fact, the catalytic activity is also influenced by the morphology and surface physiochemistry of nanosized Au, including exposed crystal surfaces and capping molecules. Surprisingly, single-atom Au showed favorable ORR/OER performance, and single-atom Au provided a nearly 100 % atomic utilization rate. However, incorporating stable and high-density Au single atoms into substrate electrocatalysts, while preventing their migration and aggregation, remains a big challenge that requires much more attention.

Au can improve the catalytic activity of most OER catalysts. This enhancement could be attributed to the unique structural characteristics of Au and its interaction with other OER catalysts. Au has the highest electronegativity among all metal elements, and the enhancement by incorporating Au with OER electrocatalysts can be classified into AEM and LOM mechanisms. In the AEM mechanism, the interfacial Au directly couples with oxygen to accelerate the kinetics of substrate OER electrocatalysts. In the LOM mechanism, the enhancement of substrate OER electrocatalysts lies in the synergistic effect between the incorporated Au and oxygen vacancies. However, it is very difficult to identify the real reaction site and reaction path because of the dynamic and irreversible reconfiguration process in the practical electrocatalytic reaction. More in situ and *operando* advanced characterization techniques are needed to monitor the structural evolution of active sites in the OER process, and further understand the interplay between incorporated Au and substrate OER electrocatalysts, which is also prospected to offer simple and accurate theoretical prediction descriptors of OER activity and stability. In conclusion, this review underscores the significant role of Au in enhancing the OER performance of various catalysts and highlights the understanding structural characteristics of Au and its interaction with other catalysts, as well as advanced characterization techniques to incorporate stable Au single atoms into substrate electrocatalysts.

CRediT authorship contribution statement

Tong Liu: Writing – original draft, Methodology, Investigation, Formal analysis, Conceptualization. **Jianwei Lu:** Writing – original draft, Methodology, Investigation, Formal analysis, Conceptualization. **Zhihao Chen:** Methodology, Investigation. **Zhihong Luo:** Methodology, Investigation. **Yurong Ren:** Methodology. **Xiangqun Zhuge:** Methodology, Investigation. **Kun Luo:** Writing – review & editing, Supervision, Project administration, Funding acquisition, Conceptualization. **Guogang Ren:** Resources. **Weiwei Lei:** Writing – review & editing, Project administration, Funding acquisition. **Dan Liu:** Writing – review & editing, Project administration, Funding acquisition, Conceptualization.

Declaration of competing interest

The authors declare that they have no known competing financial interests or personal relationships that could have appeared to influence the work reported in this paper.

Data availability

Data will be made available on request.

Acknowledgment

The authors appreciate the financial support from the National Natural Science Foundation of China (No. 51874051 and 52111530139), the Australian Research Council Discovery Program (DP220103416), and Australian Research Council Future Fellowships (FT200100730, FT210100804) and the award from the UK Royal Society (IEC\NSFC\201155, 2021-23).

References

[1] Z.P. Wu, X.F. Lu, S.Q. Zang, X.W. Lou, Non-Noble-Metal-Based Electrocatalysts toward the Oxygen Evolution Reaction, Adv. Funct. Mater. 30 (15) (2020) 1910274, https://doi.org/10.1002/adfm.201910274.

[2] Z. Luo, G. Zhu, L. Yin, F. Li, B.B. Xu, L. Dala, X. Liu, K. Luo, A Facile Surface Preservation Strategy for the Lithium Anode for High-Performance Li-O_2 Batteries, ACS Appl. Mater. Interfaces 12 (24) (2020) 27316–27326, https://doi.org/10.1021/acsami.0c08355.

[3] Z. Luo, G. Zhu, L. Guo, F. Li, Y. Li, M. Fu, Y.C. Cao, Y.L. Li, K. Luo, Improving the cyclability and capacity of Li-O_2 batteries via low rate pre-activation, Chem. Commun. (Camb) 55 (14) (2019) 2094–2097, https://doi.org/10.1039/c8cc09935a.

[4] W. Chen, Z. Luo, X. Zhuge, Z. Ding, Y. Ren, A. Loya, Y. Li, K. Luo, Protecting lithium anode with ionic liquid modified poly(vinylidene fluoride) single ion conducting separators for iodide-assisted lithium oxygen batteries, J. Storage Mater. 50 (2022) 104580, https://doi.org/10.1016/j.est.2022.104580.

[5] J. Fang, Z. Ding, Y. Ling, J. Li, X. Zhuge, Z. Luo, Y. Ren, K. Luo, Green recycling and regeneration of $LiNi_{0.5}Co_{0.2}Mn_{0.3}O_2$ from spent Lithium-ion batteries assisted by sodium sulfate electrolysis, Chem. Eng. J. 440 (2022) 135880, https://doi.org/10.1016/j.cej.2022.135880.

[6] Z.H. Luo, F.J. Li, C.L. Hu, L.K. Yin, D.G. Li, C.H. Ji, X.Q. Zhuge, K. Zhang, K. Luo, Highly dispersed silver nanoparticles for performance-enhanced lithium oxygen batteries, J. Mater. Sci. Technol. 73 (2021) 171–177, https://doi.org/10.1016/j.jmst.2020.07.039.

[7] Z. Luo, F. Li, C. Hu, D. Li, Y. Cao, K. Scott, X. Gong, K. Luo, Impact of a Gold Nanocolloid Electrolyte on Li_2O_2 Morphology and Performance of a Lithium-Oxygen Battery, ACS Appl. Mater. Interfaces 13 (3) (2021) 4062–4071, https://doi.org/10.1021/acsami.0c20871.

[8] K. Luo, G. Zhu, Y. Zhao, Z. Luo, X. Liu, K. Zhang, Y. Li, K. Scott, Enhanced cycling stability of Li–O_2 batteries by using a polyurethane/SiO_2/glass fiber nanocomposite separator, J. Mater. Chem. A 6 (17) (2018) 7770–7776, https://doi.org/10.1039/c8ta00879e.

[9] H. Mu, X. Zhuge, G. Ren, K. Luo, Z. Ding, Y. Ren, Z. Luo, M. Bayati, B.B. Xu, X. Liu, Dual functional mesoporous silica colloidal electrolyte for lithium-oxygen batteries, Chem. Eng. J. 455 (2023) 140761, https://doi.org/10.1016/j.cej.2022.140761.

[10] Z.H. Luo, L.K. Yin, L. Xiang, T.X.T. Liu, Z. Song, Y.B. Li, L. Zhou, K. Luo, K. Wu, J. J. Jiang, AuPt Nanoparticles/Multi-Walled carbon nanotubes catalyst as high active and stable oxygen reduction catalyst for Al-Air batteries, Appl. Surf. Sci. 564 (2021) 150474, https://doi.org/10.1016/j.apsusc.2021.150474.

[11] L. Xiang, Z.H. Luo, C.L. Hu, Z.C. Bian, J.W. Lu, Y.C. Cao, K. Luo, Gold Nanoparticle/Multi-walled Carbon Nanotube Hybrid as a Stable Catalyst for the Oxygen Reduction Reaction, ChemElectroChem 5 (7) (2018) 1073–1079, https://doi.org/10.1002/celc.201701311.

[12] L.L. Guo, L. Xiang, F.J. Li, X.T. Liu, L. Xing, D.G. Li, Z.H. Luo, K. Luo, Silver Nanoparticle/Multiwalled Carbon Nanotube Hybrid as an Efficient Electrocatalyst for the Oxygen Reduction Reaction in Alkaline Medium, ChemElectroChem 6 (9) (2019) 2489–2496, https://doi.org/10.1002/celc.201900232.

[13] M. Sankar, Q. He, R.V. Engel, M.A. Sainna, A.J. Logsdail, A. Roldan, D.J. Willock, N. Agarwal, C.J. Kiely, G.J. Hutchings, Role of the Support in Gold-Containing Nanoparticles as Heterogeneous Catalysts, Chem. Rev. 120 (8) (2020) 3890–3938, https://doi.org/10.1021/acs.chemrev.9b00662.

[14] M. Haruta, T. Kobayashi, H. Sano, N. Yamada, Novel Gold Catalysts for the Oxidation of Carbon Monoxide at a Temperature far Below 0 °C, Chem. Lett. 16 (2) (1987) 405–408, https://doi.org/10.1246/cl.1987.405.

[15] G.J. Hutchings, Vapor phase hydrochlorination of acetylene: Correlation of catalytic activity of supported metal chloride catalysts, J. Catal. 96 (1) (1985) 292–295, https://doi.org/10.1016/0021-9517(85)90383-5.

[16] S. Karra, M. Wooten, W. Griffith, W. Gorski, Morphology of Gold Nanoparticles and Electrocatalysis of Glucose Oxidation, Electrochim. Acta 218 (2016) 8–14, https://doi.org/10.1016/j.electacta.2016.09.097.

[17] M. Nazemi, S.R. Panikkanvalappil, M.A. El-Sayed, Enhancing the rate of electrochemical nitrogen reduction reaction for ammonia synthesis under ambient conditions using hollow gold nanocages, Nano Energy 49 (2018) 316–323, https://doi.org/10.1016/j.nanoen.2018.04.039.

[18] C. Li, O.J.H. Chai, Q. Yao, Z. Liu, L. Wang, H. Wang, J. Xie, Electrocatalysis of gold-based nanoparticles and nanoclusters, Mater. Horiz. 8 (6) (2021) 1657–1682, https://doi.org/10.1039/d0mh01947j.

[19] M. Benedet, G. Andrea Rizzi, A. Gasparotto, O.I. Lebedev, L. Girardi, C. Maccato, D. Barreca, Tailoring oxygen evolution performances of carbon nitride systems fabricated by electrophoresis through Ag and Au plasma functionalization, Chem. Eng. J. 448 (2022) 137645, https://doi.org/10.1016/j.cej.2022.137645.

[20] L. Bigiani, T. Andreu, C. Maccato, E. Fois, A. Gasparotto, C. Sada, G. Tabacchi, D. Krishnan, J. Verbeeck, J.R. Morante, D. Barreca, Engineering Au/MnO_2 hierarchical nanoarchitectures for ethanol electrochemical valorization, J. Mater. Chem. A 8 (33) (2020) 16902–16907, https://doi.org/10.1039/D0TA05972B.

[21] D. Hu, P. Diao, D. Xu, Q. Wu, Gold/WO_3 nanocomposite photoanodes for plasmonic solar water splitting, Nano Res. 9 (6) (2016) 1735–1751, https://doi.org/10.1007/s12274-016-1067-0.

[22] P.Y. Lu, J.W. Zhou, Y.K. Hu, J.W. Yin, Y.H. Wang, J.L. Yu, Y.B. Ma, Z.L. Zhu, Z. Y. Zeng, Z.X. Fan, Gold-based nanoalloys: synthetic methods and catalytic applications, J. Mater. Chem. A 9 (35) (2021) 19025–19053, https://doi.org/10.1039/d1ta03646g.

[23] X.C. Wang, Z.H. Zang, C.Y. Fan, Y.T. Zhang, X. Li, L.L. Li, X.F. Yu, X.J. Yang, Z. M. Lu, X.H. Zhang, Effects of Group IB Metals of Au/Ag/Cu on Boosting Oxygen Evolution Reaction of Cobalt Hydroxide, ChemCatChem 15 (7) (2023) 202300033, https://doi.org/10.1002/cctc.202300033.

[24] Y.Q. Sun, W.W. Cao, Y.P. Lv, X.D. Yang, W.G. Ma, Q. Shen, B.T. Kang, C.C. Li, Interface charge distribution modulation of Au@NiO Core-Shell nanoparticles for efficient oxygen evolution reaction, Appl. Surf. Sci. 637 (2023) 157870, https://doi.org/10.1016/j.apsusc.2023.157870.

[25] R. Kamar, R. Agoston, G.A. van Riessen, G. Hinsley, A.P. O'Mullane, M.W. M. Jones, Probing the effect of metal to ligand charge transfer on the oxygen evolution reaction in Au incorporated $Co(OH)_2$ thin film electrocatalysts, J. Mater. Chem. A 11 (38) (2023) 20816–20823, https://doi.org/10.1039/d3ta03923d.

[26] H. Gong, G. Sun, W. Shi, D. Li, X. Zheng, H. Shi, X. Liang, R. Yang, C. Yuan, Nano-Au-decorated hierarchical porous cobalt sulfide derived from ZIF-67 toward optimized oxygen evolution catalysis: Important roles of microstructures and electronic modulation, Carbon Energy. (2024) 432, https://doi.org/10.1002/cey2.432.

[27] D.R. Kauffman, X. Deng, D.C. Sorescu, T.-D. Nguyen-Phan, C. Wang, C.M. Marin, E. Stavitski, I. Waluyo, A. Hunt, Edge-Enhanced Oxygen Evolution Reactivity at Ultrathin, Au-Supported Fe_2O_3 Electrocatalysts, ACS Catal. 9 (6) (2019) 5375–5382, https://doi.org/10.1021/acscatal.9b01093.

[28] H. Xia, Q.F. Xie, Y.H. Tian, Q. Chen, M. Wen, J.L. Zhang, Y. Wang, Y.P. Tang, S. Zhang, High-efficient CoPt/activated functional carbon catalyst for Li-O_2 batteries, Nano Energy 84 (2021) 105877, https://doi.org/10.1016/j.nanoen.2021.105877.

[29] G. Liu, Y. Xu, T. Yang, L. Jiang, Recent advances in electrocatalysts for seawater splitting, Nano Materials Science. 5 (1) (2023) 101–116, https://doi.org/10.1016/j.nanoms.2020.12.003.

[30] J. Wang, C.-X. Zhao, J.-N. Liu, D. Ren, B.-Q. Li, J.-Q. Huang, Q. Zhang, Quantitative kinetic analysis on oxygen reduction reaction: A perspective, Nano Materials Science. 3 (3) (2021) 313–318, https://doi.org/10.1016/j.nanoms.2021.03.006.

[31] A. Ruban, B. Hammer, P. Stoltze, H.L. Skriver, J.K. Nørskov, Surface electronic structure and reactivity of transition and noble metals, J. Mol. Catal. A Chem. 115 (3) (1997) 421–429, https://doi.org/10.1016/S1381-1169(96)00348-2.

[32] J.K. Nørskov, J. Rossmeisl, A. Logadottir, L. Lindqvist, J.R. Kitchin, T. Bligaard, H. Jónsson, Origin of the Overpotential for Oxygen Reduction at a Fuel-Cell Cathode, J. Phys. Chem. B 108 (46) (2004) 17886–17892, https://doi.org/10.1021/jp047349j.

[33] J.K. Nørskov, F. Abild-Pedersen, F. Studt, T. Bligaard. Density functional theory in surface chemistry and catalysis. Proceedings of the National Academy of Sciences. 108(3) (2011) 937-943. https://doi.org/10.1073/pnas.1006652108.

[34] B. Hammer, J.K. Nørskov, Theoretical surface science and catalysis—calculations and concepts, Adv. Catal. 45 (2000) 71–129, https://doi.org/10.1016/S0360-0564(02)45013-4.

[35] J. Greeley, J.K. Nørskov, Combinatorial Density Functional Theory-Based Screening of Surface Alloys for the Oxygen Reduction Reaction, J. Phys. Chem. C 113 (12) (2009) 4932–4939, https://doi.org/10.1021/jp808945y.

[36] J. Zhang, H.B. Yang, D. Zhou, B. Liu, Adsorption Energy in Oxygen Electrocatalysis, Chem. Rev. 122 (23) (2022) 17028–17072, https://doi.org/10.1021/acs.chemrev.1c01003.

[37] L. Qin, G. Ma, L. Wang, Z. Tang, Atomically precise metal nanoclusters for (photo) electroreduction of CO_2: Recent advances, challenges and opportunities, Journal of Energy Chemistry. 57 (2021) 359–370, https://doi.org/10.1016/j.jechem.2020.09.003.

[38] H. Chen, Z. Xing, S. Zhu, L. Zhang, Q. Chang, J. Huang, W.-B. Cai, N. Kang, C.-J. Zhong, M. Shao, Palladium modified gold nanoparticles as electrocatalysts for ethanol electrooxidation, J. Power Sources 321 (2016) 264–269, https://doi.org/10.1016/j.jpowsour.2016.04.072.

[39] S. Zhu, Q. Wang, X. Qin, M. Gu, R. Tao, B.P. Lee, L. Zhang, Y. Yao, T. Li, M. Shao, Tuning Structural and Compositional Effects in Pd–Au Nanowires for Highly Selective and Active CO_2 Electrochemical Reduction Reaction, Adv. Energy Mater. 8 (32) (2018) 1802238, https://doi.org/10.1002/aenm.201802238.

[40] Y. Yang, C. Dai, A. Fisher, Y. Shen, D. Cheng, A full understanding of oxygen reduction reaction mechanism on Au(1 1 1) surface, J. Phys. Condens. Matter 29 (36) (2017) 365201, https://doi.org/10.1088/1361-648X/aa7db6.

[41] Z. Duan, G. Henkelman, Theoretical Resolution of the Exceptional Oxygen Reduction Activity of Au(100) in Alkaline Media, ACS Catal. 9 (6) (2019) 5567–5573, https://doi.org/10.1021/acscatal.9b00955.

[42] F. Lu, Y. Zhang, S. Liu, D. Lu, D. Su, M. Liu, Y. Zhang, P. Liu, J.X. Wang, R. R. Adzic, O. Gang, Surface Proton Transfer Promotes Four-Electron Oxygen Reduction on Gold Nanocrystal Surfaces in Alkaline Solution, J. Am. Chem. Soc. 139 (21) (2017) 7310–7317, https://doi.org/10.1021/jacs.7b01735.

[43] S. Balasubramanian, A. Sheelam, K. Ramanujam, R. Dhamodharan, Green, Seed-Mediated Synthesis of Au Nanowires and Their Efficient Electrocatalytic Activity in Oxygen Reduction Reaction, ACS Appl. Mater. Interfaces 9 (34) (2017) 28876–28886, https://doi.org/10.1021/acsami.7b07553.

[44] X. Jiang, X. Qiu, G. Fu, J. Sun, Z. Huang, D. Sun, L. Xu, J. Zhou, Y. Tang, Highly simple and rapid synthesis of ultrathin gold nanowires with (111)-dominant facets and enhanced electrocatalytic properties, J. Mater. Chem. A 6 (36) (2018) 17682–17687, https://doi.org/10.1039/c8ta06676k.

[45] K. Luo, H. Wang, X. Li, Electrocatalytic activity of ligand-protected gold particles: formaldehyde oxidation, Gold Bull. 47 (1–2) (2013) 41–46, https://doi.org/10.1007/s13404-013-0110-0.

[46] D.G. Li, Y.J. Luo, J.X. Lan, Z.H. Luo, F.J. Li, K. Luo, Synthesis of amphiphilic Janus gold nanoparticles stabilized with triphenylphosphine and D-penicillamine by ligand exchange at toluene/water emulsion interface, Gold Bull. 53 (2) (2020) 55–62, https://doi.org/10.1007/s13404-020-00274-1.

[47] D. Li, C. Hu, Y. Luo, G. Zhu, Q. Li, Z. Luo, K. Luo, One-pot synthesis of amphiphilic Janus gold nanoparticles with d-penicillamine and benzyl mercaptan ligands by toluene/water emulsion reaction, Appl. Surf. Sci. 475 (2019) 615–620, https://doi.org/10.1016/j.apsusc.2019.01.021.

[48] Y. Zhang, L. Hu, W. Han, Insights into in situ one-step synthesis of carbon-supported nano-particulate gold-based catalysts for efficient electrocatalytic CO_2 reduction, J. Mater. Chem. A 6 (46) (2018) 23610–23620, https://doi.org/10.1039/C8TA08698B.

[49] T. Kawawaki, Y. Negishi, Gold Nanoclusters as Electrocatalysts for Energy Conversion, Nanomaterials (basel). 10 (2020) 238, https://doi.org/10.3390/nano10020238.

[50] L. Wang, Z. Tang, W. Yan, H. Yang, Q. Wang, S. Chen, Porous Carbon-Supported Gold Nanoparticles for Oxygen Reduction Reaction: Effects of Nanoparticle Size, ACS Appl. Mater. Interfaces 8 (32) (2016) 20635–20641, https://doi.org/10.1021/acsami.6b02223.

[51] W. Chen, S. Chen, Oxygen electroreduction catalyzed by gold nanoclusters: strong core size effects, Angew. Chem. Int. Ed. Engl. 48 (24) (2009) 4386–4389, https://doi.org/10.1002/anie.200901185.

[52] B. Kumar, T. Kawawaki, N. Shimizu, Y. Imai, D. Suzuki, S. Hossain, L.V. Nair, Y. Negishi, Gold nanoclusters as electrocatalysts: size, ligands, heteroatom doping, and charge dependences, Nanoscale 12 (18) (2020) 9969–9979, https://doi.org/10.1039/d0nr00702a.

[53] L. Sumner, N.A. Sakthivel, H. Schrock, K. Artyushkova, A. Dass, S. Chakraborty, Electrocatalytic Oxygen Reduction Activities of Thiol-Protected Nanomolecules Ranging in Size from $Au_{28}(SR)_{20}$ to $Au_{279}(SR)_{84}$, J. Phys. Chem. C 122 (43) (2018) 24809–24817, https://doi.org/10.1021/acs.jpcc.8b07962.

[54] T.C. Jones, L. Sumner, G. Ramakrishna, M.b. Hatshan, A. Abuhagr, S. Chakraborty, A. Dass. Bulky t-Butyl Thiolated Gold Nanomolecular Series: Synthesis, Characterization, Optical Properties, and Electrocatalysis. The Journal of Physical Chemistry C. 122(31) (2018) 17726-17737. https://doi.org/10.1021/acs.jpcc.8b01106.

[55] Y. Lu, Y. Jiang, X. Gao, W. Chen, Charge state-dependent catalytic activity of $[Au_{25}(SC_{12}H_{25})_{18}]$ nanoclusters for the two-electron reduction of dioxygen to hydrogen peroxide, Chem. Commun. (Camb) 50 (62) (2014) 8464–8467, https://doi.org/10.1039/c4cc01841a.

[56] A. Wang, J. Li, T. Zhang, Heterogeneous single-atom catalysis, Nat. Rev. Chem. 2 (6) (2018) 65–81, https://doi.org/10.1038/s41570-018-0010-1.

[57] Y.J. Chen, S.F. Ji, C. Chen, Q. Peng, D.S. Wang, Y.D. Li, Single-Atom Catalysts: Synthetic Strategies and Electrochemical Applications, Joule. 2 (7) (2018) 1242–1264, https://doi.org/10.1016/j.joule.2018.06.019.

[58] Z. Chen, Q. Zhang, W. Chen, J. Dong, H. Yao, X. Zhang, X. Tong, D. Wang, Q. Peng, C. Chen, W. He, Y. Li, Single-Site Au_I Catalyst for Silane Oxidation with Water, Adv. Mater. 30 (5) (2018) 1704720, https://doi.org/10.1002/adma.201704720.

[59] X. Li, W. Bi, L. Zhang, S. Tao, W. Chu, Q. Zhang, Y. Luo, C. Wu, Y. Xie, Single-Atom Pt as Co-Catalyst for Enhanced Photocatalytic H_2 Evolution, Adv. Mater. 28 (12) (2016) 2427–2431, https://doi.org/10.1002/adma.201505281.

[60] G. Vilé, D. Albani, M. Nachtegaal, Z. Chen, D. Dontsova, M. Antonietti, N. López, J. Pérez-Ramírez, A Stable Single-Site Palladium Catalyst for Hydrogenations, Angew. Chem. Int. Ed. 54 (38) (2015) 11265–11269, https://doi.org/10.1002/anie.201505073.

[61] Z. Chen, Y. Chen, S. Chao, X. Dong, W. Chen, J. Luo, C. Liu, D. Wang, C. Chen, W. Li, J. Li, Y. Li, Single-Atom Au^I–N_3 Site for Acetylene Hydrochlorination Reaction, ACS Catal. 10 (3) (2020) 1865–1870, https://doi.org/10.1021/acscatal.9b05212.

[62] X. Wang, W. Wang, M. Qiao, G. Wu, W. Chen, T. Yuan, Q. Xu, M. Chen, Y. Zhang, X. Wang, J. Wang, J. Ge, X. Hong, Y. Li, Y. Wu, Y. Li, Atomically dispersed Au_1 catalyst towards efficient electrochemical synthesis of ammonia, Science Bulletin. 63 (19) (2018) 1246–1253, https://doi.org/10.1016/j.scib.2018.07.005.

[63] L.Y. Liu, H. Su, F.M. Tang, X. Zhao, Q.H. Liu, Confined organometallic Au_1N_x single-site as an efficient bifunctional oxygen electrocatalyst, Nano Energy 46 (2018) 110–116, https://doi.org/10.1016/j.nanoen.2018.01.044.

[64] T. Jing, D.M. Liang, M.S. Deng, S.H. Cai, X.S. Qi, Density Functional Theory Studies of Heteroatom-Doped Graphene-like GaN Monolayers as Electrocatalysts for Oxygen Evolution and Reduction, Acs Applied Nano Materials. 4 (7) (2021) 7125–7133, https://doi.org/10.1021/acsanm.1c01119.

[65] F.Y. Chen, Z.Y. Wu, Z. Adler, H.T. Wang, Stability challenges of electrocatalytic oxygen evolution reaction: From mechanistic understanding to reactor design, Joule. 5 (7) (2021) 1704–1731, https://doi.org/10.1016/j.joule.2021.05.005.

[66] O. Kasian, J.-P. Grote, S. Geiger, S. Cherevko, K.J.J. Mayrhofer, The Common Intermediates of Oxygen Evolution and Dissolution Reactions during Water Electrolysis on Iridium, Angew. Chem. Int. Ed. 57 (9) (2018) 2488–2491, https://doi.org/10.1002/anie.201709652.

[67] C. Wang, M. Humayun, D.P. Debecker, Y. Wu, Electrocatalytic water oxidation with layered double hydroxides confining single atoms, Coord. Chem. Rev. 478 (2023) 214973, https://doi.org/10.1016/j.ccr.2022.214973.

[68] F. Zaccaria, L. Fagiolari, A. Macchioni, Optimizing noble metals exploitation in water oxidation catalysis by their incorporation in layered double hydroxides, Inorg. Chim. Acta 516 (2021) 120161, https://doi.org/10.1016/j.ica.2020.120161.

[69] B.S. Yeo, A.T. Bell, Enhanced activity of gold-supported cobalt oxide for the electrochemical evolution of oxygen, J. Am. Chem. Soc. 133 (14) (2011) 5587–5593, https://doi.org/10.1021/ja200559j.
[70] Y. Gorlin, C.J. Chung, J.D. Benck, D. Nordlund, L. Seitz, T.C. Weng, D. Sokaras, B. M. Clemens, T.F. Jaramillo, Understanding interactions between manganese oxide and gold that lead to enhanced activity for electrocatalytic water oxidation, J. Am. Chem. Soc. 136 (13) (2014) 4920–4926, https://doi.org/10.1021/ja407581w.
[71] P.C. Chen, M.F. Li, J.B. Jin, S. Yu, S.P. Chen, C.B. Chen, M. Salmeron, P.D. Yang, Heterostructured Au-Ir Catalysts for Enhanced Oxygen Evolution Reaction, Acs Mater Lett. 3 (10) (2021) 1440–1447, https://doi.org/10.1021/acsmaterialslett.1c00428.
[72] Z.B. Ke, L.J. Li, Q.R. Jia, Y.G. Yang, H.W. Cui, Facile synthesis of jagged Au/Ir nanochains with superior electrocatalytic activity for oxygen evolution reaction, Appl. Surf. Sci. 463 (2019) 58–65, https://doi.org/10.1016/j.apsusc.2018.08.198.
[73] H. Wang, Z.N. Chen, D. Wu, M. Cao, F. Sun, H. Zhang, H. You, W. Zhuang, R. Cao, Significantly Enhanced Overall Water Splitting Performance by Partial Oxidation of Ir through Au Modification in Core-Shell Alloy Structure, J. Am. Chem. Soc. 143 (12) (2021) 4639–4645, https://doi.org/10.1021/jacs.0c12740.
[74] S. Moon, Y.B. Cho, A. Yu, M.H. Kim, C. Lee, Y. Lee, Single-Step Electrospun Ir/IrO_2 Nanofibrous Structures Decorated with Au Nanoparticles for Highly Catalytic Oxygen Evolution Reaction, ACS Appl. Mater. Interfaces 11 (2) (2019) 1979–1987, https://doi.org/10.1021/acsami.8b14563.
[75] T. Kwon, A. Yu, S.J. Kim, M.H. Kim, C. Lee, Y. Lee, Au-Ru alloy nanofibers as a highly stable and active bifunctional electrocatalyst for acidic water splitting, Appl. Surf. Sci. 563 (2021) 150293, https://doi.org/10.1016/j.apsusc.2021.150293.
[76] Z. Fan, Z. Luo, Y. Chen, J. Wang, B. Li, Y. Zong, H. Zhang, Synthesis of 4H/fcc-Au@M (M = Ir, Os, IrOs) Core-Shell Nanoribbons For Electrocatalytic Oxygen Evolution Reaction, Small 12 (29) (2016) 3908–3913, https://doi.org/10.1002/smll.201601787.
[77] H. Li, C. Chen, D.F. Yan, Y.Y. Wang, R. Chen, Y.Q. Zou, S.Y. Wang, Interfacial effects in supported catalysts for electrocatalysis, J. Mater. Chem. A 7 (41) (2019) 23432–23450, https://doi.org/10.1039/c9ta04888j.
[78] C.C. Cheng, P.Y. Cheng, C.L. Huang, D.S. Raja, Y.J. Wu, S.Y. Lu, Gold nanocrystal decorated trimetallic metal organic frameworks as high performance electrocatalysts for oxygen evolution reaction, Appl Catal B-Environ. 286 (2021) 119916, https://doi.org/10.1016/j.apcatb.2021.119916.
[79] I. Vassalini, L. Borgese, M. Mariz, S. Polizzi, G. Aquilanti, P. Ghigna, A. Sartorel, V. Amendola, I. Alessandri, Enhanced Electrocatalytic Oxygen Evolution in Au-Fe Nanoalloys, Angew. Chem. Int. Ed. Engl. 56 (23) (2017) 6589–6593, https://doi.org/10.1002/anie.201703387.
[80] R. Sanchis-Gual, T.F. Otero, M. Coronado-Puchau, E. Coronado, Enhancing the electrocatalytic activity and stability of Prussian blue analogues by increasing their electroactive sites through the introduction of Au nanoparticles, Nanoscale 13 (29) (2021) 12676–12686, https://doi.org/10.1039/d1nr02928b.
[81] Z. Zhuang, W. Sheng, Y. Yan, Synthesis of monodispere Au@Co_3O_4 core-shell nanocrystals and their enhanced catalytic activity for oxygen evolution reaction, Adv. Mater. 26 (23) (2014) 3950–3955, https://doi.org/10.1002/adma.201400336.
[82] A.L. Strickler, M.A. Escudero-Escribano, T.F. Jaramillo, Core-Shell Au@Metal-Oxide Nanoparticle Electrocatalysts for Enhanced Oxygen Evolution, Nano Lett. 17 (10) (2017) 6040–6046, https://doi.org/10.1021/acs.nanolett.7b02357.
[83] J.Y. Zhang, B.A. Guo, J. Liang, L. Zou, J. Lu, J.X. Liu, Au-Doped CuO_x Nanoparticles as Electrocatalysts for Oxygen Evolution Reaction, Acs Applied Nano Materials. 5 (5) (2022) 6500–6504, https://doi.org/10.1021/acsanm.2c00528.
[84] S.Y. Zhang, J.J. Ma, H.L. Zhu, Y.Q. Zheng, Self-supported beaded Au@Co_3O_4 nanowire arrays perform electrocatalytic CO_2 reduction in water to syngas and water oxidation to O_2, New J. Chem. 44 (27) (2020) 11808–11816, https://doi.org/10.1039/d0nj02179b.
[85] W.Y. Zhang, H.M. Guan, Y.F. Hu, W. Wang, X.L. Yang, C.Y. Kuang, Enhancing catalytic activity of Fe_3O_4 for electrochemical water oxidation via the coupling of OER-inert Au, Int J Hydrogen Energ. 47 (54) (2022) 22731–22737, https://doi.org/10.1016/j.ijhydene.2022.05.100.
[86] L. Bigiani, A. Gasparotto, T. Andreu, J. Verbeeck, C. Sada, E. Modin, O.I. Lebedev, J.R. Morante, D. Barreca, C. Maccato, Au–Manganese Oxide Nanostructures by a Plasma-Assisted Process as Electrocatalysts for Oxygen Evolution: A Chemico-Physical Investigation, Advanced Sustainable Systems. 5 (11) (2020) 2000177, https://doi.org/10.1002/adsu.202000177.
[87] P. Muthukumar, P. Ranganathan, M. Pannipara, A.G. Al-Sehemi, S.P. Anthony, Highly Enhanced OER Activity of Amorphous Co_3O_4 via Fabricating Hybrid Amorphous-Crystalline Gold Nanostructures, ChemistrySelect 5 (30) (2020) 9357–9361, https://doi.org/10.1002/slct.202002248.
[88] R. Frydendal, L.C. Seitz, D. Sokaras, T.C. Weng, D. Nordlund, I. Chorkendorff, I.E. L. Stephens, T.F. Jaramillo, Operando investigation of Au-MnO_x thin films with improved activity for the oxygen evolution reaction, Electrochim. Acta 230 (2017) 22–28, https://doi.org/10.1016/j.electacta.2017.01.085.
[89] Y.Y. Fang, X.Z. Li, Y.P. Hu, F. Li, X.Q. Lin, M. Tian, X.C. An, Y. Fu, J. Jin, J.T. Ma, Ultrasonication-assisted ultrafast preparation of multiwalled carbon nanotubes/Au/Co_3O_4 tubular hybrids as superior anode materials for oxygen evolution reaction, J. Power Sources 300 (2015) 285–293, https://doi.org/10.1016/j.jpowsour.2015.09.049.
[90] C.H. Kuo, W. Li, L. Pahalagedara, A.M. El-Sawy, D. Kriz, N. Genz, C. Guild, T. Ressler, S.L. Suib, J. He, Understanding the role of gold nanoparticles in enhancing the catalytic activity of manganese oxides in water oxidation reactions, Angew. Chem. Int. Ed. Engl. 54 (8) (2015) 2345–2350, https://doi.org/10.1002/anie.201407783.
[91] G.X. Zhu, X.Y. Li, Y.J. Liu, W.J. Zhu, X.P. Shen, Activating $CoFe_2O_4$ electrocatalysts by trace Au for enhanced oxygen evolution activity, Appl. Surf. Sci. 478 (2019) 206–212, https://doi.org/10.1016/j.apsusc.2019.01.241.
[92] H. Cheng, C.Y. Su, Z.Y. Tan, S.Z. Tai, Z.Q. Liu, Interacting $ZnCo_2O_4$ and Au nanodots on carbon nanotubes as highly efficient water oxidation electrocatalyst, J. Power Sources 357 (2017) 1–10, https://doi.org/10.1016/j.jpowsour.2017.04.091.
[93] M.A. Sayeed, T. Herd, A.P. O'Mullane, Direct electrochemical formation of nanostructured amorphous $Co(OH)_2$ on gold electrodes with enhanced activity for the oxygen evolution reaction, J. Mater. Chem. A 4 (3) (2016) 991–999, https://doi.org/10.1039/c5ta09125j.
[94] C. Cai, S. Han, X. Zhang, J. Yu, X. Xiang, J. Yang, L. Qiao, X. Zu, Y. Chen, S. Li, Ultrahigh oxygen evolution reaction activity in Au doped co-based nanosheets, RSC Adv. 12 (10) (2022) 6205–6213, https://doi.org/10.1039/d1ra09094a.
[95] R. Madhu, A. Karmakar, K. Karthick, S. Sam Sankar, S. Kumaravel, K. Bera, S. Kundu, Metallic Gold-Incorporated $Ni(OH)_2$ for Enhanced Water Oxidation in an Alkaline Medium: A Simple Wet-Chemical Approach, Inorg. Chem. 60 (20) (2021) 15818–15829, https://doi.org/10.1021/acs.inorgchem.1c02571.
[96] Y. Zhou, H.C. Zeng, Metal-hydroxide and gold-nanocluster interfaces: enhancing catalyst activity and stability for oxygen evolution reaction, J. Phys. Chem. C 120 (51) (2016) 29348–29357, https://doi.org/10.1021/acs.jpcc.6b11102.
[97] D. Zhang, L. Peng, Z. Yang, Y. Yang, H. Li, Gold-Supported Nanostructured NiFeCoPr hydroxide as a high-performance supercapacitor electrode and electrocatalyst toward the oxygen evolution reaction, Inorg. Chem. 58 (23) (2019) 15841–15852, https://doi.org/10.1021/acs.inorgchem.9b02230.
[98] R. Cai, H.Y. Jin, D. Yang, K.T. Lin, K. Chan, J.K. Sun, Z. Chen, X.B. Zhang, W. H. Tan, Generalized preparation of Au NP @ $Ni(OH)_2$ yolk-shell NPs and their enhanced catalytic activity, Nano Energy 71 (2020) 104542, https://doi.org/10.1016/j.nanoen.2020.104542.
[99] P. Muthukumar, S.P. Anthony, Gold doping induced strong enhancement of carbon quantum dots fluorescence and oxygen evolution reaction catalytic activity of amorphous cobalt hydroxide, New J. Chem. 42 (23) (2018) 18794–18801, https://doi.org/10.1039/c8nj04429e.
[100] B. Sidhureddy, A.R. Thiruppathi, A.C. Chen, Au nanoparticle incorporated Co$(OH)_2$ hybrid thin film with high electrocatalytic activity and stability for overall water splitting, J. Electroanal. Chem. 794 (2017) 28–35, https://doi.org/10.1016/j.jelechem.2017.04.003.
[101] X. Liu, S.J. Jing, C.G. Ban, K.W. Wang, Y.J. Feng, C. Wang, J.J. Ding, B. Zhang, K. Zhou, L.Y. Gan, X.Y. Zhou, Dynamic active sites in NiFe oxyhydroxide upon Au nanoparticles decoration for highly efficient electrochemical water oxidation, Nano Energy 98 (2022) 107328, https://doi.org/10.1016/j.nanoen.2022.107328.
[102] J.S. Sun, Y.T. Zhou, R.Q. Yao, H. Shi, Z. Wen, X.Y. Lang, Q. Jiang, Nanoporous gold supported chromium-doped NiFe oxyhydroxides as high-performance catalysts for the oxygen evolution reaction, J. Mater. Chem. A 7 (16) (2019) 9690–9697, https://doi.org/10.1039/c9ta01027k.
[103] W. Zhu, L. Liu, Z. Yue, W. Zhang, X. Yue, J. Wang, S. Yu, L. Wang, J. Wang, Au promoted nickel-iron layered double hydroxide nanoarrays: a modular catalyst enabling high-performance oxygen evolution, ACS Appl. Mater. Interfaces 9 (23) (2017) 19807–19814, https://doi.org/10.1021/acsami.7b03033.
[104] J. Zhang, J. Liu, L. Xi, Y. Yu, N. Chen, S. Sun, W. Wang, K.M. Lange, B. Zhang, Single-atom Au/NiFe layered double hydroxide electrocatalyst: probing the origin of activity for oxygen evolution reaction, J. Am. Chem. Soc. 140 (11) (2018) 3876–3879, https://doi.org/10.1021/jacs.8b00752.
[105] S. Kitano, T.G. Noguchi, M. Nishihara, K. Kamitani, T. Sugiyama, S. Yoshioka, T. Miwa, K. Yoshizawa, A. Staykov, M. Yamauchi, Heterointerface created on Au-cluster-loaded unilamellar hydroxide electrocatalysts as a highly active site for the oxygen evolution reaction, Adv. Mater. 34 (16) (2022) 2110552, https://doi.org/10.1002/adma.202110552.
[106] E. Havakeshian, H. Salavati, M. Taei, F. Hasheminasab, M. Seddighi, Enhanced activity of CaFeMg layered double hydroxides-supported gold nanodendrites for the electrochemical evolution of oxygen and hydrogen in alkaline media, Chem. Phys. Lett. 693 (2018) 46–54, https://doi.org/10.1016/j.cplett.2017.12.076.
[107] M. Taei, E. Havakeshian, F. Hasheminasab, A gold nanodendrite-decorated layered double hydroxide as a bifunctional electrocatalyst for hydrogen and oxygen evolution reactions in alkaline media, RSC Adv. 7 (74) (2017) 47049–47055, https://doi.org/10.1039/c7ra05625g.
[108] N.M. Tran, S. Kim, H. Yoo, Gold nanodot assembly within a cobalt chalcogenide nanoshell: Promotion of electrocatalytic activity, J. Colloid Interface Sci. 605 (2022) 274–285, https://doi.org/10.1016/j.jcis.2021.07.075.
[109] H.D. Mai, V.C.T. Le, H. Yoo, Effective fabrication and electrochemical oxygen evolution reaction activity of gold multipod nanoparticle core-cobalt sulfide shell nanohybrids, Acs Applied Nano Materials. 2 (2) (2019) 678–688, https://doi.org/10.1021/acsanm.8b01689.
[110] Y. Lv, S. Duan, Y. Zhu, P. Yin, A.R. Wang, Enhanced OER Performances of Au@$NiCo_2S_4$ Core-Shell Heterostructure, Nanomaterials (basel). 10 (2020) 611, https://doi.org/10.3390/nano10040611.
[111] S.B. Duan, Y.P. Lv, P. Yin, Y.C. Zhu, R.M. Wang, Constructing the Au-$CoNi_2S_4$ core-shell heterostructure to promote the catalytic performance for oxygen evolution, J. Phys. D Appl. Phys. 54 (42) (2021) 425501, https://doi.org/10.1088/1361-6463/ac0de7.
[112] S. Javaid, X.M. Xu, W. Chen, J.Y. Chen, H.Y. Hsu, S. Wang, X.Y. Yang, Y.G. Li, Z. P. Shao, F. Jones, G.H. Jia, Ni^{2+}/Co^{2+} doped Au-Fe_7S_8 nanoplatelets with

exceptionally high oxygen evolution reaction activity, Nano Energy 89 (2021) 106463, https://doi.org/10.1016/j.nanoen.2021.106463.
[113] H. Liu, J.N. Cheng, W.J. He, Y. Li, J. Mao, X.R. Zheng, C. Chen, C.X. Cui, Q.Y. Hao, Interfacial electronic modulation of Ni_3S_2 nanosheet arrays decorated with Au nanoparticles boosts overall water splitting, Appl Catal B-Environ. 304 (2022) 120935, https://doi.org/10.1016/j.apcatb.2021.120935.
[114] C. Cai, S. Han, Q. Wang, M. Gu, Direct observation of yolk-shell transforming to gold single atoms and clusters with superior oxygen evolution reaction efficiency, ACS Nano 13 (8) (2019) 8865–8871, https://doi.org/10.1021/acsnano.9b02135.
[115] Y.Y. Xu, S.B. Duan, H.Y. Li, M. Yang, S.J. Wang, X. Wang, R.M. Wang, Au/$Ni_{12}P_5$ core/shell single-crystal nanoparticles as oxygen evolution reaction catalyst, Nano Res. 10 (9) (2017) 3103–3112, https://doi.org/10.1007/s12274-017-1527-1.
[116] X. Zhang, A. Shan, S. Duan, H. Zhao, R. Wang, W.M. Lau, Au@Co_2P core/shell nanoparticles as a nano-electrocatalyst for enhancing the oxygen evolution reaction, RSC Adv. 9 (70) (2019) 40811–40818, https://doi.org/10.1039/c9ra07535f.
[117] M.Y. Lv, Y. Zhou, S.A. Rasaki, H.J. Shen, C.X. Wang, W.Y. Song, T. Thomas, M. H. Yang, J. Wang, Gold nanocluster-decorated nickel nitride as stable electrocatalyst for oxygen evolution reaction in alkaline media, ChemElectroChem 6 (22) (2019) 5744–5749, https://doi.org/10.1002/celc.201901439.
[118] D.C. Nguyen, T.L.L. Doan, S. Prabhakaran, D.H. Kim, N.H. Kim, J.H. Lee, Rational construction of Au@$Co_2N_{0.67}$ nanodots-interspersed 3D interconnected N-graphene hollow sphere network for efficient water splitting and Zn-air battery, Nano Energy 89 (2021) 106420, https://doi.org/10.1016/j.nanoen.2021.106420.
[119] R.Q. Yao, H. Shi, W.B. Wan, Z. Wen, X.Y. Lang, Q. Jiang, Flexible Co-Mo-N/Au electrodes with a hierarchical nanoporous architecture as highly efficient electrocatalysts for oxygen evolution reaction, Adv. Mater. 32 (10) (2020) 1907214, https://doi.org/10.1002/adma.201907214.
[120] X. Zhao, P.F. Gao, Y. Yan, X.Q. Li, Y.L. Xing, H.L. Li, Z.M. Peng, J.L. Yang, J. Zeng, Gold atom-decorated $CoSe_2$ nanobelts with engineered active sites for enhanced oxygen evolution, J. Mater. Chem. A 5 (38) (2017) 20202–20207, https://doi.org/10.1039/c7ta06172b.
[121] S. Zhao, R. Jin, H. Abroshan, C. Zeng, H. Zhang, S.D. House, E. Gottlieb, H.J. Kim, J.C. Yang, R. Jin, Gold Nanoclusters Promote Electrocatalytic Water Oxidation at the Nanocluster/$CoSe_2$ Interface, J. Am. Chem. Soc. 139 (3) (2017) 1077–1080, https://doi.org/10.1021/jacs.6b12529.
[122] W. Yuan, Y. Ma, H. Wu, L. Cheng, Single-atom catalysts for CO oxidation, CO_2 reduction, and O_2 electrochemistry, Journal of Energy Chemistry. 65 (2022) 254–279, https://doi.org/10.1016/j.jechem.2021.05.046.
[123] N. Zhang, Y. Chai, Lattice oxygen redox chemistry in solid-state electrocatalysts for water oxidation, Energ. Environ. Sci. 14 (9) (2021) 4647–4671, https://doi.org/10.1039/D1EE01277K.
[124] A. Grimaud, O. Diaz-Morales, B. Han, W.T. Hong, Y.L. Lee, L. Giordano, K. A. Stoerzinger, M.T.M. Koper, Y. Shao-Horn, Activating lattice oxygen redox reactions in metal oxides to catalyse oxygen evolution, Nat. Chem. 9 (5) (2017) 457–465, https://doi.org/10.1038/nchem.2695.
[125] Z.-F. Huang, J. Song, Y. Du, S. Xi, S. Dou, J.M.V. Nsanzimana, C. Wang, Z.J. Xu, X. Wang, Chemical and structural origin of lattice oxygen oxidation in Co–Zn oxyhydroxide oxygen evolution electrocatalysts, Nat. Energy 4 (4) (2019) 329–338, https://doi.org/10.1038/s41560-019-0355-9.
[126] N. Zhang, X. Feng, D. Rao, X. Deng, L. Cai, B. Qiu, R. Long, Y. Xiong, Y. Lu, Y. Chai, Lattice oxygen activation enabled by high-valence metal sites for enhanced water oxidation, Nat. Commun. 11 (1) (2020) 4066, https://doi.org/10.1038/s41467-020-17934-7.
[127] H. Zhang, P. Li, H.C. Zhou, J.M. Xu, Q.F. Jiang, J.H.L. Hadden, Y.Y. Wang, M. N. Wang, S.L. Chen, F. Xie, J. Riley, Unravelling the synergy of oxygen vacancies and gold nanostars in hematite for the electrochemical and photoelectrochemical oxygen evolution reaction, Nano Energy 94 (2022) 106968, https://doi.org/10.1016/j.nanoen.2022.106968.
[128] H. Zhong, Q. Zhang, J. Yu, X. Zhang, C. Wu, Y. Ma, H. An, H. Wang, J. Zhang, X. Wang, J. Xue, Fundamental understanding of structural reconstruction behaviors in oxygen evolution reaction electrocatalysts, Adv. Energy Mater. (2023) 2301391, https://doi.org/10.1002/aenm.202301391.